

Separation of Sodium Signals Between Mono- and Bi-Exponential T₂ Decays via Multi-TE Single-Quantum Sodium (²³Na) MRI

Yongxian Qian,¹ Ying-Chia Lin,¹ Xingye Chen,^{1,2} Tiejun Zhao,³ Karthik Lakshmanan,¹ Yulin Ge,¹ Yvonne W. Lui,^{1,4} Fernando E. Boada^{1,5}

¹ Bernard and Irene Schwartz Center for Biomedical Imaging, Department of Radiology, New York University Grossman School of Medicine, New York, NY 10016.

² Vilcek Institute of Graduate Biomedical Sciences, NYU Grossman School of Medicine, New York, NY 10016.

³ Siemens Medical Solutions USA, New York, NY 10016.

⁴ Department of Radiology, NYU Langone Health, New York, NY 10016.

⁵ Now at Department of Radiology, Stanford University, Stanford, CA 94305.

Running title: Mono- and bi-T2 sodium separation

Manuscript type: Research Article

Word Count (body): 5451

Key Words: sodium MRI, single-quantum MRI, triple-quantum MRI, neuroimaging, neurodegeneration

Correspondence: Yongxian Qian, PhD

Center for Biomedical Imaging (CBI)

660 First Ave, 4th Floor

New York, NY 10016, USA

Phone: 212-263-1159

Email: Yongxian.Qian@nyulangone.org

This work was partially presented in the 25th Annual Meeting of ISMRM, Honolulu, Hawaii, USA, 2017.

NIH-Funding Required Statement: Research reported in this publication was supported in part by the National Institute On Aging of the National Institutes of Health under Award Number

R01AG067502. The content is solely the responsibility of the authors and does not necessarily represent the official views of the National Institutes of Health.

Financial support: This work was financially supported in part by the National Institutes of Health (NIH) RF1/R01 AG067502, RF1 NS110041, R01 NS113517, R01 NS108491, and R01 CA111996; and by the General Research Fund from the Department of Radiology, New York University Grossman School of Medicine. This work was also performed under the rubric of the Center for Advanced Imaging Innovation and Research (CAI2R, www.cai2r.net), an NIBIB Biomedical Technology Resource Center (NIH P41 EB017183).

ABSTRACT

Purpose: It is a long-standing pursuit in sodium (^{23}Na) MRI to separate signals between mono- and bi-exponential T_2 decays in the human brain, due to lack of clinically-translational solutions under the restriction of intrinsically low signal-to-noise ratio (SNR). Here we propose a new technique called multi-TE single-quantum (MSQ) sodium MRI to address the challenge.

Methods: We exploit an intrinsic difference in T_2 decay between mono- and bi-exponential sodium signals by acquiring SQ images at multiple TEs and performing voxel-based matrix inversions on these SQ images. The MSQ method was then investigated on numerical models, agar phantoms, and human brains for the feasibility on clinical scanners at 3T.

Results: The whole brain T_2^* spectrum of FID signals from the study subjects showed sparse peaks (2–4 peaks), suggesting a global set of T_2^* values ($T_2^*_{\text{fr}}$, $T_2^*_{\text{bs}}$, $T_2^*_{\text{bl}}$) applicable to the separation. The simulations indicated a small impact (3.9–5.6%) of T_2^* variation on accuracy of the separation, and the phantom experiments showed a high accuracy of the separation, 95.8% for mono- T_2 sodium and 72.5–80.4% for bi- T_2 sodium. The human studies demonstrated feasibility of the separation and potentials of highlighting abnormal brain regions in the bi- T_2 sodium images.

Conclusion: The MSQ technique has been shown, via the numerical simulations, phantom experiments, and human brain studies, to be able to separate mono- and bi- T_2 sodium signals using a two-TE sampling scheme and a global set of T_2^* values. However, MSQ has limitations and requires cautions in practice.

Keywords: sodium MRI, single-quantum MRI, triple-quantum MRI, neuroimaging, neurodegeneration

1. INTRODUCTION

In human brains, sodium ions (Na^+), when exposed to an electric field gradient of negatively charged macromolecules and proteins, experience nuclear quadrupolar interaction that results in bi-exponential decay in transverse (T_2) relaxation of nuclear spins when the ions are not in fast motion, a situation in which correlation time between sodium ions and electric field gradient is much shorter than the inverse of Larmor frequency, $\tau_c \ll 1/\omega_0$.^{1,2} Sodium ions in fast motion cancel out the effect of quadrupolar interactions, resulting in mono-exponential T_2 decay.¹⁻⁴ Sodium ions in bi-exponential T_2 decay were historically, but incorrectly, considered as invisible “bound” (chemically) sodium^{5,6} because their short- T_2 components were not detectable by then-NMR (nuclear magnetic resonance) techniques.¹⁻⁴ The terminology however remains in use in today’s sodium MRI, although concerns have been raised recently by some researchers, with no better substitutes yet.⁷ For convenience, this article refers “bound” (not chemically) sodium to those showing bi-exponential T_2 decay and “free” sodium to those showing mono-exponential T_2 decay. The free and bound sodium ions can appear in both intra- and extra-cellular spaces,⁸⁻¹⁰ depending on their relative correlation time with electric field gradient.^{1,2}

Sodium (^{23}Na) MRI currently acquires signals from both free and bound sodium ions, and quantifies total sodium concentration (TSC) at voxels of an image. TSC is unique measure for non-invasive assessment of disruption in ionic homeostasis of cells in, or recovery from, pathological conditions such as stroke, tumor, multiple sclerosis, epilepsy, bipolar disorder, and mild traumatic brain injury.⁸⁻¹² However, TSC is dominated by free sodium from cerebrospinal fluid (CSF) which has a high sodium concentration (~ 145 mM) and overshadows alteration in intracellular sodium which has a much lower concentration (~ 15 mM). Separation of mono- and bi- T_2 sodium signals can remove CSF impact and highlight intracellular alterations, especially at early stage of a disease happening at cellular level or in early (cellular) response to a treatment.

The difference in T_2 relaxation was extensively explored in sodium MRI as a means to separate the two populations of sodium in the brain. Triple quantum filtering (TQF) was considered a standard for human studies, in which MR signals were generated solely from triple-quantum (TQ) transitions.¹³ TQF techniques, however, require multiple radiofrequency (RF) pulses for excitation and multi-step phase cycling to eliminate single-quantum (SQ) signals,¹³⁻¹⁷ leading to long scan time (20–40 min) and high specific absorption rate (SAR, causing a safety concern).

More problematic is that TQF has much low signal-to-noise ratio (SNR) about 10 times lower than SQ.¹⁵⁻¹⁷ These difficulties hamper TQF to be widely used on humans.

Alternative approaches were proposed. Inversion recovery (IR), adopted from proton (¹H) MRI, exploits a difference in T₁ relaxation between the mono- and bi-T₂ sodium ions, and suppresses signals from the mono-T₂ sodium of longer T₁ time.¹⁸⁻²⁰ The IR approach needs an extra RF pulse for the suppression and worsens SAR issue, not favorable to human studies. It also suffers from incomplete suppression of the mono-T₂ sodium signals which are ~10 times higher than the bi-T₂ sodium signals, due to spatial inhomogeneity of B₁⁺ field although adiabatic pulses are usually used, and complicates quantification of the bi-T₂ sodium owing to unknown residual mono-T₂ sodium signals.^{9,11,18} To overcome these drawbacks, another alternative approach, called short-T₂ imaging, was proposed in which SQ images were acquired at multiple echo times (TEs) and then subtracted from each other to produce an image of the short-T₂ component of bi-T₂ sodium.²¹⁻²⁴ In such a way, SAR was reduced to, and SNR was increased to, the level of SQ images, favorable to human studies in clinic. Unfortunately, the subtraction could not completely eliminate mono-T₂ sodium signal (~20% in residual), degrading accuracy of bi-T₂ sodium quantification.²⁴

In this study, the short-T₂ imaging is generalized to multi-TE single-quantum (MSQ) imaging to improve accuracy of the separation between mono- and bi-T₂ sodium signals, by replacing the subtraction with a matrix inversion. To develop MSQ technique, we optimized the TEs for data acquisition, investigated impact of T₂ values on accuracy of the separation, and acquired the free induction decay (FID) signals to generate T₂* spectrum for the matrix equation. To test MSQ technique, we implemented numerical simulations, phantom studies, and human studies. The results were supportive of the proposed MSQ technique. We also itemized limitations of MSQ technique and potential pitfalls in interpretation of separated sodium signals.

2. THEORY

2.1. Model of sodium signals

A two-population model is used to describe single-quantum sodium signal $m(t)$ evolving with time t at an imaging voxel ΔV .

$$m(t) = m_{fr} Y_{fr}(t) + m_{bd} Y_{bd}(t), \quad t \geq 0 \quad \text{Eq. [1a]}$$

$$m_{fr} \geq 0, m_{bd} \geq 0, \text{ and } m_{fr} + m_{bd} = m(0)$$

$$Y_{fr}(t) \equiv \exp(-t/T_{2,fr}) \quad \text{Eq. [1b]}$$

$$Y_{bd}(t) \equiv a_{bs} \exp(-t/T_{2,bs}) + a_{bl} \exp(-t/T_{2,bl}) \quad \text{Eq. [1c]}$$

m_{fr} and m_{bd} are signal intensity proportional to volume fraction v_q and sodium concentration C_q , i.e., $m_q \propto \Delta V(v_q C_q)$, $q=fr$ and bd , for the mono- T_2 (or free) and bi- T_2 (or bound) sodium populations in a voxel ΔV , respectively. $Y_{fr}(t)$ is relaxation decay of the free sodium of time constant $T_{2,fr}$, and $Y_{bd}(t)$ is relaxation decay of the bound sodium with $a_{bs} = 0.6$ for the short- T_2 component ($T_{2,bs}$) and $a_{bl} = 0.4$ for the long- T_2 component ($T_{2,bl}$). The split of 60% vs. 40% in intensity is from theoretical and experimental results for individual sodium nuclear spins.^{1-4,49} The T_2 values are in an order of $T_{2,bs} \ll T_{2,bl} \leq T_{2,fr}$. Model Eq. 1 doesn't include free sodium of short T_2 .

2.2. Separation of the mono- and bi- T_2 sodium signals

Given SQ sodium images at $\{TE_1, TE_2, \dots, TE_N\}$, Eq. 1a becomes a matrix equation Eq. 2.

$$\mathbf{M} = \mathbf{Y} \mathbf{X} \quad \text{Eq. [2a]}$$

$$\mathbf{M} \equiv (m_1, m_2, \dots, m_N)^T, \quad m_i = m(TE_i), i = 1, 2, \dots, N \quad \text{Eq. [2b]}$$

$$\mathbf{X} \equiv (m_{fr}, m_{bd})^T \quad \text{Eq. [2c]}$$

$$\mathbf{Y} \equiv \begin{pmatrix} Y_{fr}(TE_1) & Y_{bd}(TE_1) \\ Y_{fr}(TE_2) & Y_{bd}(TE_2) \\ \vdots & \vdots \\ Y_{fr}(TE_N) & Y_{bd}(TE_N) \end{pmatrix} \quad \text{Eq. [2d]}$$

Superscript T is operator for matrix transpose. A solution to Eq. 2 is given by Eq. 3 via an established algorithm called non-negative least-squares (NNLS)²⁵ in which non-negative condition on \mathbf{X} is incorporated into the solution.

$$\mathbf{X} = \text{NNLS}(\mathbf{Y}\mathbf{X} - \mathbf{M}) \quad \text{Eq. [3]}$$

2.3. Measurement of T_2 values for the mono- and bi- T_2 sodium populations

The T_2 values ($T_{2,fr}$, $T_{2,bs}$, $T_{2,bl}$) in Eqs. 1b and 1c are required to perform the separation. They can be measured by acquiring FID signal $s(t)$ on whole imaging volume and using effective T_2 (i.e., T_2^*) decay model of multi-exponential components to fit the FID signal in magnitude, i.e.,

$$|s(t)| = \sum_j A_j \exp(-t/T_{2,j}^*) \quad \text{Eq. [4]}$$

Hereinafter, T_2^* replaces T_2 as spin echo is not favorable to sodium MRI. The curve-fitting is accomplished also through the NNLS algorithm²⁵ when T_2^* values are pre-distributed in a range

of interest $[T_2^{*\min}, T_2^{*\max}]$ at uniform or non-uniform intervals $\{\Delta T_{2,j}^*, j = 1, 2, \dots\}$. Amplitudes $\{A_j\}$, called T_2^* spectrum, determine relative incidence of T_2^* components in the imaging volume which counts all T_2^* components from both mono- and bi- T_2 sodium populations. To pair up the short- and long- T_2^* components of the bi- T_2 sodium, the 60-40 split in intensity is a helpful guidance.

Alternatively, empirical estimates of the brain tissues may be applicable to T_2^* values, because solutions to Eq. 2 are not so sensitive to T_2^* values due to exponential decay (see Sections 2.4 and 4.2 for details).

FID signals, when acquired with an array coil, may have unique initial phases $\{\varphi_{0,l}, l=1, 2, \dots, N_c\}$ at individual elements, and need to be aligned to produce a resultant FID signal. Alignment (via phase correction) can be towards a reference phase such as zero phase, one of the initial phases, or mean phase across elements. In addition, signal intensity at individual elements needs to be scaled via ‘‘FFT factor’’ which is stored in the header of a raw FID data file.

FID signals at the first few samples are distorted by hardware filtering during analog-to-digital conversion (ADC). The number of affected samples are in a range of 3–10 points, depending on sampling bandwidth, with the first sample having the largest distortion. This distortion alters measurement of T_2^* components, especially the short T_2^* components which are critically important to the bi- T_2 sodium. Correction for the distortion can be performed using an established exponential extrapolation (see Appendix A for details).

2.4. Impact of T_2^* values on the mono- and bi- T_2 sodium separation

Ideally, T_2^* values are measured at individual voxels. Practically, the measurement is time consuming and not favorable in clinical studies. A fast estimate is necessary. Intuitively, solutions $\{m_{fr}, m_{bd}\}$ to Eq. 1 are not very sensitive to T_2^* values due to exponential decays in Eqs. 1b and 1c. This observation can be verified theoretically and numerically. Theoretically, small changes in T_2^* values, $\{\delta T_{2,q}^*, q=fr, bs, bl\}$, lead to small changes $\{\delta m_p, p=fr, bd\}$ in m_{fr} and m_{bd} under the same $m(t)$, that is,

$$0 = \delta(m_{fr}Y_{fr}) + \delta(m_{bd}Y_{bd}) \quad \text{Eq. [5a]}$$

$$-m_\delta = Y_{fr}\delta m_{fr} + Y_{bd}\delta m_{bd} \quad \text{Eq. [5b]}$$

$$m_\delta \equiv m_{fr}\delta Y_{fr} + m_{bd}\delta Y_{bd} \quad \text{Eq. [5c]}$$

$$\delta Y_q = \left(\frac{tY_q}{T_{2,q}^*} \right) \left(\frac{\delta T_{2,q}^*}{T_{2,q}^*} \right) \leq e^{-1} \left(\frac{\delta T_{2,q}^*}{T_{2,q}^*} \right), \quad q=fr, bs, bl \quad \text{Eq. [5d]}$$

$$\delta Y_{bd} = a_{bs} \delta Y_{bs} + a_{bl} \delta Y_{bl} \leq e^{-1} \left[a_{bs} \left(\frac{\delta T_{2,bs}^*}{T_{2,bs}^*} \right) + a_{bl} \left(\frac{\delta T_{2,bl}^*}{T_{2,bl}^*} \right) \right] \quad \text{Eq. [5e]}$$

Where δ is difference operator.

Numerically, errors in m_{fr} and m_{bd} can be calculated, given a series of $\{T_{2,q}^*, \delta T_{2,q}^*; q=fr, bs, bl\}$ at a specific pair (m_{fr}, m_{bd}) . This creates a plot showing how the computed (m_{fr}, m_{bd}) change with $\{\delta T_{2,q}^*; q=fr, bs, bl\}$.

2.5. Optimization of the number of TEs

In principle, the more TEs the better differentiation between the T_2^* relaxations of the mono- and bi- T_2 sodium populations, and the better solutions to Eq. 2. In practice, the number of TEs is restricted by total scan time (TA), SNR, signal decay, and risk of motion artifacts across TEs. Therefore, a trade-off must be made for the number of TEs. To determine an optimal number of TEs, it is necessary to understand noise propagation in Eq. 2. Let singular value decomposition (SVD)²⁶ of the matrix \mathbf{Y} in Eq. 2a be

$$\mathbf{Y} = \mathbf{U} \mathbf{\Sigma} \mathbf{V}^T \quad \text{Eq. [6a]}$$

$$\mathbf{\Sigma} = \text{diag}(\sigma_1, \sigma_2) \quad \text{Eq. [6b]}$$

$$\mathbf{X} = \mathbf{V} \mathbf{\Sigma}^{-1} \mathbf{U}^T \mathbf{M} \quad \text{Eq. [6c]}$$

Singular values (σ_1, σ_2) determine noise transfer (amplification or suppression) in Eq. 6c from the measured TE-images \mathbf{M} to the separated mono- and bi- T_2 sodium images \mathbf{X} .

However, Eq. 6c allows negative values in \mathbf{X} when random noise contaminates \mathbf{M} . This violates the “non-negative” condition on \mathbf{X} . Therefore, SVD analysis is applicable only to \mathbf{X} elements with $\text{SNR} \geq 2$ where the elements, with Gaussian noise, have 95.4% of chance in the territory of non-negative value.²⁷

3. METHODS

The proposed MSQ technique is graphically illustrated in Fig. 1. The inputs are multiple TE images and an FID signal. The outputs are the mono- T_2 (free), bi- T_2 (bound), and total sodium images, as well as the map of field inhomogeneity ΔB_0 and the map of single- T_2^* . In between are the data

processing functionalities for the T_2^* spectrum, mono- and bi- T_2 sodium separation, and mapping of ΔB_0 and single- T_2^* . Motion correction (MoCo) across multi-TE images is optional. Also optional is the low-pass (LP) filtering, which is a 3D averaging over a size of $3 \times 3 \times 3$ voxels for instance, to reduce random noise on the bi- T_2 sodium. The ΔB_0 and single- T_2^* maps present spatial distributions of the B_0 field inhomogeneity and the short- and long- T_2^* components, and provide indications for uncertain short- T_2^* decays possibly caused by the B_0 inhomogeneity. These maps are critical and complimentary to quantification and explanation of the separated mono- and bi- T_2 sodium signals.

To implement the MSQ technique, a computer software was custom-developed in MATLAB (R2021a, MathWorks, Natick, MA) on a laptop computer (MacBook Pro, 16GB memory, Apple M1 chip, Apple Inc., Cupertino, CA).

The numerical simulations in this study were performed in MATLAB on the MacBook Pro laptop or Windows desktop, otherwise specified. Random noise of Gaussian distribution was generated using MATLAB function $randn(n)$, while the NNLS algorithm was implemented using $[x, resnorm, residual] = lsqnonneg(C, d)$.

3.1. Measurement of T_2^* values

FID signals were acquired on whole brain of the study subjects right before sodium imaging. A product pulse sequence, either *AdjXFre* embedded in the manual shimming task or independent *fid_23Na*, was employed with parameters: TE=0.35–1.0ms, TR=100–300ms, and averages =1–128, and TA=0.2–39s. When a dual-tuned (^1H - ^{23}Na) 8-channel Tx/Rx head array coil²⁸ was used, there was a difference in initial phase and in FFT scale factors across channels. The initial phases were measured on channel image at central slice, and removed by aligning to zero phase. Channel signals were weighted with FFT scale factors and complex-value combined into a resultant FID. An additional step was performed to correct for distortion at the first few points of the resultant FID signal. Finally, a spectrum of T_2^* values was calculated according to Eq. 4, at a resolution of 0.5ms for T_2^* in 0.5–100ms. Assignment of T_2^* peaks to $\{T_2^*_{\text{fr}}, T_2^*_{\text{bs}}, T_2^*_{\text{bl}}\}$ was based on their relative positions and intensities, i.e., $T_2^*_{\text{fr}} \geq T_2^*_{\text{bl}} \gg T_2^*_{\text{bs}}$ and intensity ratio 6:4 for the bi- T_2 sodium. Repeatability of the T_2^* measurement is addressed in the Supporting Information.

3.2. Sensitivity to T_2^* values

As a testing, a set of T_2^* values, $\{T_{2,fr}^*, T_{2,bs}^*, T_{2,bl}^*\} = \{50.0, 3.5, 15.0\}$ ms, most commonly encountered in our human brain studies, was employed. Then, an error of $\delta T_{2,q}^*$, $q=fr, bs, bl$, in a range of $\pm 20\%$ was added to the testing values. Finally, $\{m_{fr}, m_{bd}\}$ and errors $\{\delta m_{fr}, \delta m_{bd}\}$ relative to the true values in a range of $0.1 \leq m_{fr} \leq 0.9$, were calculated according to Eq. 3. The relationships between $\{\delta m_{fr}, \delta m_{bd}\}$ and $\{\delta T_{2,q}^*; q=fr, bs, bl\}$ were plotted. To focus on the relation of “ $\delta T_2^* - \delta m$ ”, TEs were sampled in an ideal case, i.e., $TE_0 = 0$, $\Delta TE = 1$ ms, and 80 TEs covering entire T_2^* decays.

3.3. Optimization of TEs

The simulations were implemented via Eq. 6 for three cases: an ideal case serving as reference, practical case 1 having a large number of TEs, and practical case 2 having a small number of TEs. The ideal case had 80 TEs, i.e., $TE = (0, 1, 2, \dots, 79)$ ms, to cover entire range of T_2^* decays. The two practical cases, suggested by existing human studies,^{24,29-31} had total scan time (TA) limited to 22min for 8 TE-images, and the TEs were chosen to be most sensitive to T_2^* decays.²⁹ Thus, the case 1 had 8 TEs = (0.5, 1, 2, 3, 4, 5, 7, 10) ms, and the case 2 only had two TEs = (0.5, 5.0) ms but 4 averages at each TE. The SVD singular values ($\sigma_1 \geq \sigma_2 \geq 0$) were calculated for each set of TEs via Eq. 6. The optimal set of TEs would be the one that had σ_2 producing the minimum amplification of random noise in the separated mono- and bi- T_2 sodium images.

3.4. Computer simulations

The mono- and bi- T_2 sodium separation was carried out via Eq. 3 at a typical set of T_2^* values, $(T_{2,fr}^*, T_{2,bs}^*, T_{2,bl}^*) = (50.0, 3.5, 15.0)$ ms, and an optimal two-TE scheme, $TE = (0.5, 5.0)$ ms. Sodium signals were calculated via Eq. 1, with an additive Gaussian noise, $N(0, \sigma^2)$, at each of noise trials (independent from each other), $m(t) + n(t)$. The mono- and bi- T_2 signal amplitudes $\{m_{fr}, m_{bd}\}$ were simulated to vary in a normalized range of 0.0–1.0 at a step size = 0.1. The separation was implemented using the function *lsqnonneg()* in MATLAB, and repeated N_{noise} times at each of the specific amplitudes. Mean and standard deviation (SD) were reported as separated sodium signal. $N_{\text{noise}} = 1054$ was chosen to detect a 10% of SD, or 0.1 effect size $d = \Delta\mu/\text{SD}$, in difference between the mean and true value at 90% power and 5% significant level under the two-sided Student's *t*-test.²⁷

3.5. Phantom studies

Four phantoms, custom-built and described in previous work,²⁴ were studied. They were 50-mL centrifuge tubes filled with a mixture of distilled water, 10% w/w agar powder, and sodium chloride (NaCl) at three concentrations (90, 120, and 150mM) and at 150mM without agar, mimicking bi- and mono-T₂ sodium signals in the brain tissues. Sodium MRI was performed on a clinical scanner at 3T (MAGNETOM Trio Tim, Siemens Medical Solutions, Erlangen, Germany) with a dual-tuned (¹H-²³Na) volume head coil (Advanced Imaging Research, Cleveland, OH). The data acquisition was implemented using an SNR-efficient, three-dimensional (3D) pulse sequence called the twisted projection imaging (TPI),³² with parameters: rectangular RF pulse duration = 0.8ms, flip angle=80° (limited by SAR and TR), field of view (FOV)=220mm, matrix size=64, nominal resolution=3.44mm (3D isotropic), TPI readout time=36.32ms, total TPI projections =1596, TPI *p*-factor=0.4, TR=100ms, TE₁/TE₂=0.5/5ms, averages=4, and TA=10.64min per TE-image. The image reconstruction was offline implemented on a desktop computer (OptiPlex 7050, 8GB memory, Windows 10, DELL, Round Rock, TX) using a custom-developed programs in C++ (MS Visual Studio 2012, Microsoft, Redmond, WA). Separation of the mono- and bi-T₂ sodium signals was implemented using a custom-developed program as described above.

3.6. Human studies

The human studies were conducted with the approval of local Institutional Review Board (IRB) at NYU Grossman School of Medicine, New York, NY, USA. The study subjects included nine healthy adults (age 39.6±21.4 years between 21–74 years; 3 males and 6 females) and six patients with diverse neurological disorders (1 bipolar disorder, 3 epilepsy, 1 multiple sclerosis, and 1 mild traumatic brain injury; age 30.5±15.1 years between 18–59 years; 3 males and 3 females), after the exclusion of one subject and one patient due to motion between the two TE-images. The study was performed on a clinical 3T MRI scanner (Prisma, Siemens Healthineers, Erlangen, Germany) with a custom-built 8-channel dual-tuned (¹H-²³Na) head array coil.²⁸ The same TPI pulse sequence as in the phantom studies was used for data acquisition. Images were reconstructed using the gridding algorithm,^{33,34} off-line and channel-by-channel, and combined into a resultant image via the sum-of-squares (SOS) algorithm.³⁵ To decouple random noise across channels, an orthogonal linear transform (detailed in Ref. 30) was performed in which physical channel data

were transformed into virtual channels with random noise independent from channel to channel. This decoupling and denoising process also normalized signal amplitudes across channels by dividing noise standard deviation. Separation of the mono- and bi-T₂ sodium signals was implemented in the same way as in the phantom studies.

3.7. Mapping of ΔB_0 and single-T₂*

To map ΔB_0 (or $\Delta f_0 = \gamma \Delta B_0 / 2\pi$), Hermitian product method³⁶ was performed via Eq. 7 at individual imaging voxels to calculate phase differences $\{\Delta\varphi_i, i = 1, 2, \dots, N - 1\}$ between TEs $\{TE_i, i = 1, 2, \dots, N\}$. Image amplitude at individual channels were corrected with the FFT factors $\{w_l, l = 1, 2, \dots, N_c\}$. Phase unwrapping was not performed due to small intervals in the TEs and, in general, small inhomogeneity in the B_0 field in sodium MRI. Computation for ΔB_0 map is fast (0.078s) on a Mac laptop computer for images of size $64 \times 64 \times 64$ at two TEs.

$$\Delta f_0 = \frac{1}{2\pi(N-1)} \sum_{i=1}^{N-1} \Delta\varphi_i / \Delta TE_i \quad \text{Eq. [7a]}$$

$$\Delta\varphi_i = \text{phase}\{\sum_{l=1}^{N_c} w_l^2 \cdot m_l^*(TE_i) \cdot m_l(TE_{i+1})\} \quad \text{Eq. [7b]}$$

$$\Delta TE_i = TE_{i+1} - TE_i \quad \text{Eq. [7c]}$$

To map single-T₂*, a MATLAB curve-fitting function $\text{fit}(x, y, 'exp1')$ was used to calculate single-T₂* values at each voxel via Eq. 8. A restriction ($T_{2^*_{\max}} < 100\text{ms}$) was enforced to exclude unreasonable values caused by noise. The computation time is acceptable (10min17s).

$$|m(TE_i)| = A_0 \exp(-TE_i / T_2^*), \quad 0 \leq T_2^* \leq T_{2^*_{\max}} \quad \text{Eq. [8]}$$

3.8. Signal-to-noise ratio

In a region of interest (ROI), SNR was calculated via Eq. 9 in a simplified way for both volume and array coils by taking the ratio of mean intensity S to noise standard deviation (SD) in noise-only background regions. A factor of 0.655 was applied to noise SD to account for Rician distribution in magnitude images.³⁷ For SNR mapping, pixel signal is used in the calculation.

$$SNR = 0.655 S / SD \quad \text{Eq. [9]}$$

3.9. Estimation of extra- and intracellular volume fractions

The estimates give the up-band of volume fractions when all the mono-T₂ sodium are assigned to extracellular space while the bi-T₂ sodium to intracellular space, in the case that mono- and bi-T₂

sodium may co-exist in both extra- and intracellular spaces. The estimates were made in ROIs of the gray and white matters via Eq. 10 at the concentrations $C_{ex}=145\text{mM}$ for extracellular and $C_{in}=15\text{mM}$ for intracellular spaces.

$$V_{ex} = 1/(1 + a) \quad \text{Eq. [10a]}$$

$$V_{in} = a/(1 + a) \quad \text{Eq. [10b]}$$

$$a \equiv m_{bd}C_{ex}/m_{fr}C_{in} \quad \text{Eq. [10c]}$$

3.10. Statistical Significance

A regular statistical significance ($P=0.05$) was applied to the comparisons, via Student's *t*-test, between the two sets of data in this work. Minimum sample size for the *t*-test is 16, with 80% power, 5% significance level, two-sided test, and 1.0 effect size.²⁷

4. RESULTS

4.1. Measurement of T_2^* values

Fig. 2 presents a representative of T_2^* values on a healthy subject (52 years old, male), with and without correction for the distortion at the first five ADC samples (Figs. 2a1,b1). The correction removed distortion and reduced overall residual fitting error from 2.33% to 1.49% (Figs. 2a2,b2). The correction also improved resolution of short- T_2^* components: from singlet at 2.5ms to doublet at 0.5ms and 2.5ms (Figs. 2a3,b3). A high resolution in T_2^* was achieved at 0.5ms, with residual fitting error less than 1.5%. Notably, a few of sparse peaks appear in the T_2^* spectrum, indicating that T_2^* values are well clustered in the human brain and that a single set of T_2^* values is applicable to the separation of mono- and bi- T_2 sodium.

4.2. Sensitivity to T_2^* values

Fig. 3 shows the computed impact of T_2^* values on the accuracy of separation of the mono- and bi- T_2 sodium signals (m_{fr} , m_{bd}). The calculation was performed at a typical set of $(T_2^*_{fr}, T_2^*_{bs}, T_2^*_{bl}) = (50.0, 3.5, 15.0)$ ms in two extreme cases: the mono- T_2 sodium dominating, $m_{fr} = 0.9$, and the bi- T_2 sodium dominating, $m_{bd} = 0.9$. The impact of individual T_2^* components are shown in columns. In column A, an error in $T_2^*_{fr}$ caused an error in m_{fr} or m_{bd} much smaller for the dominant one (e.g., $\Delta m_{bd} < 2.2\%$ when $\Delta T_2^*_{fr} < 20\%$, and $\Delta m_{fr} < 2.9\%$ when $\Delta T_2^*_{fr} < 5.0\%$). In column B,

an error in $T_2^*_{bs}$ had a small impact on both m_{fr} and m_{bd} (e.g., when dominating, $\Delta m_{bd} < 4.8\%$ and $\Delta m_{fr} < 0.04\%$ when $\Delta T_2^*_{bs} < 20\%$). In column C, an error in $T_2^*_{bl}$ led to an error in m_{fr} or m_{bd} much smaller for the dominant one (e.g., $\Delta m_{bd} < 5.2\%$ and $\Delta m_{fr} < 0.6\%$ when $\Delta T_2^*_{bl} < 20\%$). The best case is in column B where the $T_2^*_{bs}$ had small impact ($< 4.9\%$) on both mono- and bi- T_2 sodium signals. The worst case is in Fig. 3a1 where the $T_2^*_{fr}$ had a large impact on the bi- T_2 sodium signal, $\Delta m_{bd} = 35.6\%$ when $\Delta T_2^*_{fr} = -5\%$. In other words, when the mono- T_2 sodium is very dominating, $T_2^*_{fr}$ value should be as accurate as possible (usually achievable in practice) to attain the best separation for the bi- T_2 sodium.

4.3. Optimization of TEs

The ideal scheme of 80 TEs is presented in Fig. 4a on $Y_{fr}(TE)$ of the free sodium at a typical $T_2^*_{fr}=50\text{ms}$ and on $Y_{bd}(TE)$ of the bound sodium at a typical $\{T_2^*_{bs}, T_2^*_{bl}\} = \{3.5, 15.0\}\text{ms}$. The intuitively-favorable scheme of 8 TEs was presented in Fig. 4b, while the optimal candidate of two TEs was presented in Fig. 4c. Singular values (σ_1, σ_2) of the three TE schemes were compared against each other in Fig. 4d. In Fig. 4e is singular values of the 2-TE scheme, slowly changing with the TE_2 increasing. The σ_2 is less than 1.0 for the 8-TE and 2-TE schemes, leading to an amplification of noise. Therefore, a better choice for less noise amplification is the 2-TE scheme, in which TE_2 at 5ms produced a value near maximum of σ_2 while preserving higher signal than the larger TE_2 . Thus, the 2-TE scheme is selected for the human studies.

4.4. Computer simulations

Fig. 5 demonstrates the simulated separation of mono- and bi- T_2 sodium signals (m_{fr}, m_{bd}) at a typical set of $(T_2^*_{fr}, T_2^*_{bs}, T_2^*_{bl}) = (50.0, 3.5, 15.0)$ ms and two-TE scheme $TEs=(0.5, 5.0)$, at three SNRs: extra-high (100), high (50), and regular (25). The mean and standard deviation (SD) of the separated m_{fr} and m_{bd} were presented. The SD (error bar) consistently decreased with SNR increasing. There was an underestimate for m_{fr} or m_{bd} near the maximum value 1.0, but an overestimate near the minimum value 0.0, with an amount decreasing with SNR increasing.

4.5. Phantom studies

Fig. 6 summarizes the outcomes of phantom studies. Fig. 6a shows phantom arrangement of four tubes and sodium images at $TE_1/TE_2=0.5/5\text{ms}$. Fig. 6b shows FID signal from the four tubes at

averages=1, the residual fitting error, and the T_2^* spectrum. Fig. 6c are the sodium images separated at $(T_2^{*fr}, T_2^{*bs}, T_2^{*bl}) = (50, 5, 25)$ ms according to the T_2^* spectrum in Fig. 6b3; the maps of ΔB_0 , single- T_2^* , and SNR; the signal intensities of the separated sodium signals (mean \pm SD) in the tubes; and the quantification of sodium concentration.

The separation in Fig. 6c3 recovered 95.8% of mono- T_2 sodium signal in the saline water tube, while leaving 4.2% to bi- T_2 sodium signal (much better than 20% left by the subtraction approach²⁴). The separation recovered 72.5, 80.4, and 75.9% of bi- T_2 sodium signal in the agar tubes at sodium concentrations of 150, 120, and 90mM, respectively. The quantification of sodium concentration in Fig. 6c4, when calibrated at the saline water, showed a systematic bias in total and bi- T_2 sodium concentrations, leading to an underestimate of sodium concentrations.

4.6. Human studies

4.6.1. T_2^* values in whole brain across subjects

Fig. 7. presents a scattering plot of individual T_2^* components from the T_2^* spectra across all the subjects studied. Typical T_2^* spectra and FID signals are shown in Fig. 7a for a healthy young subject (21 years old, male) and in Fig. 7c for an epilepsy patient (31 years old, male). The peaks in the T_2^* spectra were sparse and just 2–4 peaks, suggesting that a global set of T_2^* values (T_2^{*fr} , T_2^{*bs} , T_2^{*bl}) be a plausible estimate for the whole brain (Figs. 7a, c). However, these T_2^* values are slightly different from subject to subject (Fig. 7b). The short- T_2^* component is clearly crowded in a range of 1-5ms, while the long- T_2^* is widely scattered in three bands centered at 10, 20, and 30ms, respectively. Interestingly, the long- T_2^* component is shifted to lower values in the patient group, compared with the healthy group. There seems no difference between males and females in the healthy group. Therefore, the T_2^* values are heterogeneous across the subjects.

4.6.2. Mono- and bi- T_2 sodium separation

Figs. 8 and 9 present two typical cases of the human studies in full implementation of the mono- and bi- T_2 sodium separation. Case 1 (Fig. 8) is from a 26-year-old healthy female, and includes 3D sodium images of the brain at $TE_1/TE_2=0.3/5$ ms (Fig. 8a), FID signal of whole brain and associated fitting error and T_2^* spectrum (Fig. 8b), the separated sodium images from the two-TE images using $(T_2^{*fr}, T_2^{*bs}, T_2^{*bl}) = (50.0, 6.0, 19.0)$ ms (Figs. 8c1-c3), and inverse-contrast displays (Figs. 8c4-c5). In Fig. 8d are SNR, ΔB_0 , and single- T_2^* maps calculated from the two-TE

images in Fig. 8a. Case 2 (Fig. 9) is from a 59-year-old male patient with bipolar disorder. The separated sodium images were attained at $(T_2^{*fr}, T_2^{*bs}, T_2^{*bl}) = (50.0, 2.5, 7.0)$ ms according to the peaks in Fig. 9b3.

Fig. 8 indicates that signals from CSF in the brain were effectively separated into the mono- T_2 sodium image (Fig. 8c2 or c4), while signals from brain tissues such as gray and white matters were separated into the bi- T_2 sodium image (Fig. 8c3 or c5). Notably and surprisingly, signal intensity across brain tissues looks more uniform in the bi- T_2 sodium images than in the mono- T_2 sodium images (Fig. 8c2), total sodium images (Fig. 8c1), and TE_1 -images (Fig. 8a1). SNR in Fig. 8d1 are 25+ in most regions of the brain, assuring a robust separation as suggested in the simulations in Fig. 5. The field inhomogeneity ΔB_0 in Fig. 8d2 varied between ± 20 Hz across the brain, with the largest off-resonance in the prefrontal and occipital lobes, leading to visible blurring of the tissues in the bi- T_2 sodium images (Fig. 8c3 or c5, sagittal). The single- T_2^* map in Fig. 8d3 provides a spatial distribution of short and long T_2^* components across the brain, complementary to T_2^* spectrum in Fig. 8b3. It also indicates that majority of long T_2^* components are located in the prefrontal lobe in this particular case (Fig. 8d3, sagittal).

Fig. 9 demonstrates potential benefits from the bi- T_2 sodium images of patients with neurological disorders such as bipolar disorder which is known to cause abnormally-high intracellular sodium concentration in the brain but locations are unknown.^{38,39} The bi- T_2 sodium images (Fig. 9c3 or c5) clearly highlighted brain regions of an elevated bi- T_2 sodium signal against surrounding tissues, with a ratio of 1.78 vs. 1.40 (or 27.1% increase) before the separation (Fig. 9c1). These regions have no visible contrast in the total or TE_1 -images (Fig. 9a1 or c1). SNR in these regions is 40+ (Fig. 9d1), supporting a robust separation. The field inhomogeneity ΔB_0 in these regions is low (< 5 Hz, Fig. 9d2), excluding field-induced artifacts. The single- T_2^* map in Fig. 9d3 shows abnormally low T_2^* values in these regions, confirming an increase in short- T_2^* components.

4.6.3. Estimates of extra- and intracellular volume fractions

In the healthy group (Fig. 10), the difference in volume fraction between the gray and white matters is significant ($P=0.023$): 89.6 ± 4.5 % vs. 94.0 ± 2.6 % for the intracellular space (in line with the literature, 75% vs. 92%⁸), and 10.4 ± 4.5 % vs. 6.0 ± 2.6 % for the extracellular space. No significant

difference ($P=0.953$) was found between the healthy and patient groups due to small samples ($n=9$ and 6).

5. DISCUSSION

The proposed MSQ technique has been demonstrated, using the computer simulations, physical phantoms, and human subjects, to be able to separate mono- and bi- T_2 sodium signals voxel-wise. The physics behind the technique is the intrinsic difference in T_2 relaxation between sodium nuclear spins: mono- vs. bi-exponential decay. In the restriction of total scan time, the two-TE scheme, instead of the eight-TEs, was selected for smaller transfer of random noise during the separation (Fig. 4). The measurement of T_2^* spectrum from FID signals of entire brain and the application of a global set of T_2^* values (T_2^{*fr} , T_2^{*bs} , T_2^{*bl}) were tested feasible to humans. In case of not plausible for a global set of T_2^* values (i.e., T_2^* spatially varying substantially⁴⁰⁻⁴⁷), multi-regional sets, or a linear combination of them, may be used.

The quantification of sodium concentration after the separation is not addressed in this study because it is involved in a complicated procedure of 1) calibration that transforms sodium signal into concentration and 2) correction for inhomogeneous sensitivity of coil elements. These processes deserve a separate study to deal with.

The limitations of MSQ technique are obvious, and understanding them is crucial to practice of the technique. The first limitation is the two-component model (mono- and bi- T_2 populations) which is of risk to produce a false-positive error for bi- T_2 sodium. If there are mono- and bi- T_2 sodium populations in a voxel, then they are separable. If not, such as two mono- T_2 sodium decays at different T_2^* values in a voxel, they would be falsely separated into bi- T_2 sodium because they can be combined mathematically (not physically) into a bi-exponential decay mimicking a true bi- T_2 sodium decay. This kind of false positive error stems from the fact that the separation is based on *mathematical* model, instead of *physical* model as does the TQF separation. Understanding this kind of false positive errors is critical to proper interpretation of the separated bi- T_2 sodium signals.

The second limitation is the misguided separation of single mono- T_2 sodium component of short T_2^* value in a voxel, such as regions in nose and sinuses (Figs. 8c3 and 9c3). In this

situation, the MSQ separates it into bi- T_2 sodium of underestimated intensity. These mis-separated regions can be identified by means of the maps of ΔB_0 and single- T_2^* (Figs. 8d and 9d).

The third limitation is the underestimate of bi- T_2 sodium signal caused by the TE_1 image, as illustrated in the phantom study (Fig. 6c3). The separation (Eq. 2) assumes TE_1 -image intensity exactly at TE_1 (i.e., a very short readout time). Actual TE_1 -image intensity is an average over readout time during which short- T_2^* components decay significantly when readout is relatively long, such as readout $T_s=36.32\text{ms}$ about ten times long of a short- T_2^* at 3ms in this study. Therefore, the underestimation alters with readout time or pulse sequence. To mitigate the problem, two strategies may apply. One is to replace TE_1 value in Eq. 2 with an effective (larger) value that accounts for short- T_2^* decay during the readout. The other is to shift $T_2^*_{bs}$ to a larger value, as did in previous work on the phantoms.⁴⁸ Alternatively, correction for the underestimates is integrated into calibration of image intensity for sodium concentration (Fig. 6c4).

6. CONCLUSION

The data presented in this study have demonstrated the feasibility of proposed multi-TE single-quantum sodium MRI technique to separate between mono- and bi- T_2 sodium signals in a fashion of voxel by voxel. The MSQ technique is based on a solid physics related to the intrinsic difference in T_2 relaxation between the two populations of sodium nuclear spins. The two-TE sampling scheme stands out for smaller noise transfer during the separation. A global set of T_2^* values ($T_2^*_{fr}$, $T_2^*_{bs}$, $T_2^*_{bl}$) measured on T_2^* spectrum of whole brain was tested applicable to humans. However, the MSQ technique has limitations and requires cautions in practice.

7. ACKNOWLEDGMENTS

This work was partially presented in the 25th Annual Meeting of ISMRM 2017, Honolulu, Hawaii, USA. The authors would like to thank colleagues Dr. Ryan Brown for his support in the development of the 8-channel array sodium coil and Dr. Timothy Shepherd for his support in the recruitment of epilepsy patients. This work was financially supported in part by the National Institutes of Health (NIH) RF1/R01 AG067502, RF1 NS110041, R01 NS113517, R01 NS108491, and R01 CA111996; and by the General Research Fund from the Department of Radiology, NYU Grossman School of Medicine. This work was also performed under the rubric of the Center for

Advanced Imaging Innovation and Research, an NIBIB Biomedical Technology Resource Center (NIH P41 EB017183). Specially, the research reported in this publication was supported by the National Institute on Aging of the National Institutes of Health under Award Number RF1/R01AG067502. The content is solely the responsibility of the authors and does not necessarily represent the official views of the National Institutes of Health.

8. APPENDIX A: Extrapolation of N -term exponential decay

We once accidentally read a reference in literature about this topic, but could not find the citation at hand, thus summarize here the algorithm in our own language, specifically for the recovery of FID signals. If a signal $f(t)$ is an N -term exponential decay as defined in Eq. A1 with parameters $\{A_i, b_i; i = 1, 2, \dots, N\}$, and is sampled at a uniform interval Δt , then a sample $f(t_0)$ at time t_0 can be represented by a linear combination of its late-time neighboring samples $\{f(t_0 + j\Delta t), j = 1, 2, \dots, M\}$, as shown in Eq. A2, with coefficients $\{a_j, j = 1, 2, \dots, M \geq N\}$ to be determined.

$$f(t) = \sum_{i=1}^N A_i e^{-t \cdot b_i} \quad \text{Eq. [A1]}$$

$$f(t_0) = \sum_{j=1}^M a_j f(t_0 + j\Delta t) \quad \text{Eq. [A2]}$$

Proof. Extending $f(t_0 + j\Delta t)$ in Eq. A2 according Eq. A1 gives

$$\begin{aligned} f(t_0) &= \sum_{j=1}^M a_j \left[\sum_{i=1}^N (A_i e^{-t_0 \cdot b_i}) (e^{-j\Delta t \cdot b_i}) \right] \\ &= \sum_{i=1}^N A_i e^{-t_0 \cdot b_i} \left(\sum_{j=1}^M a_j e^{-j\Delta t \cdot b_i} \right). \end{aligned} \quad \text{Eq. [A3]}$$

Select time-invariant coefficients $\{a_j, j = 1, 2, \dots, M > N\}$ to satisfy Eq. A4, thus Eq. A2 holds.

$$\sum_{j=1}^M a_j e^{-j\Delta t \cdot b_i} = 1, \text{ for } i = 1, 2, \dots, N. \quad \text{Eq. [A4]}$$

Note. The descriptions above are for backward extrapolation in time and used in the recovery of FID signal. The forward extrapolation also holds if Δt is replaced with $-\Delta t$ in Eqs. A2–A4. To find the unknown coefficients $\{a_j, j = 1, 2, \dots, M\}$, Eq. A2, instead of Eq. A4, is usually used on such a segment of $f(t)$ that it is not distorted and involves all the N exponential decays. The number of data samples on the segment should be larger than M to form an over-determined problem in case of random noise existing in the signal $f(t)$.

9. DATA AVAILABILITY STATEMENT

Upon written request, the data (sodium images and FID signals) and the software codes presented in this work are available to those solely for scientific research purposes.

10. REFERENCES

1. Hubbard PS. Nonexponential nuclear magnetic relaxation by quadrupole interaction. *J Chem Phys.* 1970; 53:985–987.
2. Jaccard G, Wimperis S, Bodenhausen G. Multiple-quantum NMR spectroscopy of $S=3/2$ spins in isotropic phase: A new probe for multiexponential relaxation. *J Chem Phys.* 1986; 85:6282–6293.
3. Shporer M, Civan MM. Nuclear magnetic resonance of sodium-23 linoleate-water. Basis for an alternative interpretation of sodium-23 spectra within cells. *Biophys J.* 1972; 12:114–122.
4. Andrasko J. Nonexponential relaxation of $^{23}\text{Na}^+$ in agarose gels. *J Magn Reson.* 1974; 16:502–504.
5. Cope F. NMR evidence for complexing of Na^+ in muscle, kidney, and brain, and by actomyosin. The relation of cellular complexing of Na^+ to water structure and to transport kinetics. *J Gen Physiol.* 1967; 50:1353–1375.
6. Sterk H, Schrunner H. On the discrimination of bound and free sodium ions in solutions of biomolecules by means of the T1 relaxation. *J Mol Liq.* 1985; 30:1781–183.
7. Burstein D, Springer Jr CS. Sodium MRI revisited. *Magn Reson Med.* 2019; 82(2):521–524.
8. Winkler SS. Sodium-23 magnetic resonance brain imaging. *Neuroradiology.* 1990; 32:416-420.
9. Hilal SK, Maudsley AA, Ra JB, Simon HE, Roschmann P, Wittekoek, Cho ZH, Mun SK. In vivo NMR imaging of sodium-23 in the human head. *J Comput Assist Tomogr.* 1985; 9:1–7.
10. Perman WH, Turski PA, Houston LW, Glover GH, Hayes CE. Methodology of in vivo human sodium MR imaging at 1.5 T. *Radiology.* 1986; 160:811-820.
11. Thulborn KR. Quantitative sodium MR imaging: A review of its evolving role in medicine. *NeuroImage.* 2018; 168:250–268.
12. Bottomley PA. Sodium MRI in man: technique and findings. *eMagRes.* 2012;1(2):353-365.
13. Chung C, Wimperis S. Optimum detection of spin-3/2 biexponential relaxation using multiple-quantum filtration techniques. *J Magn Reson.* 1990; 88:440–447.
14. Navon G. Complete elimination of the extracellular ^{23}Na NMR signal in triple quantum filtered spectra of rat heart in the presence of shift reagents. *Magn Reson Med.* 1993; 30:503–506.

15. Reddy R, Shinnar M, Wang Z, Leigh JS. Multiple-quantum filters of spin-3/2 with pulses of arbitrary flip angle. *J Magn Reson.* 1994; 104:148–152.
16. Hancu I, Boada FE, Shen GX. Three-dimensional triple-quantum-filtered ^{23}Na imaging of in vivo human brain. *Magn Reson Med.* 1999; 42:1146–1154.
17. Tsang A, Stobbe RW, Beaulieu C. Triple-quantum-filtered sodium imaging of the human brain at 4.7T. *Magn Reson Med.* 2012; 67:1633–1643.
18. Stobbe R, Beaulieu C. In vivo sodium magnetic resonance imaging of the human brain using soft inversion recovery fluid attenuation. *Magn Reson Med.* 2005; 54:1305–1310.
19. Rong P, Regatte RR, Jerschow A. Clean demarcation of cartilage tissue ^{23}Na by inversion recovery. *J Magn Reson.* 2008; 193:207–209.
20. Mennecke AB, Nagel AM, Huhn K, Linker RA, Schmidt M, Rothhammer V, Wilferth T, Linz P, Wegmann J, Eisenhut F, Engelhorn T. Longitudinal sodium MRI of multiple sclerosis lesions: Is there added value of sodium inversion recovery MRI. *J Magn Reson Imaging.* 2022; 55:140–151.
21. Ra JB, Hilal SK, Cho ZH. A method for in vivo MR imaging of the short T2 component of sodium-23. *Magn Reson Med* 1986; 3:296-302.
22. Ra JB, Hilal SK, Oh CH. An algorithm for MR imaging of the short T2 fraction of sodium using the FID signal. *J Comput Assist Tomogr* 1989; 13:302-309.
23. Benkhedah N, Bachert P, Nagel AM. Two-pulse biexponential weighted ^{23}Na imaging. *J Magn Reson.* 2014; 240:67–76.
24. Qian Y, Panigrahy A, Laymon CM, Lee VK, Drappatz J, Lieberman FS, Boada FE, Mountz JM. Short- T_2 imaging for quantifying concentration of sodium (^{23}Na) of bi-exponential T_2 relaxation. *Magn Reson Med.* 2015; 74:162–174.
25. Lawson CL, Hanson RJ. *Solving Least-Squares Problems.* Upper Saddle River: Prentice Hall; 1974. Chapter 23, p.161.
26. Golub GH, Van Loan CF. *Matrix computations (3rd Ed).* Baltimore: The John Hopkins University Press; 1996. 694 p.
27. Kirkwood BR, Sterne JAC. *Essential medical statistics.* Malden (MA, USA): Blackwell Science Ltd; 2003.
28. Lakshmanan K, Brown R, Madelin G, Qian Y, Boada F, Wiggins GC. An eight-channel sodium/proton coil for brain MRI at 3 T. *NMR Biomed.* 2018; 31:e3867.

29. Qian Y, Williams AA, Chu CR, Boada FE. Multi-component T_2^* mapping of knee cartilage with ultrashort echo time acquisitions: Ex vivo results. *Magn Reson Med.* 2010; 64:1427–1432.
30. Qian Y, Zhao T, Wiggins GC, Wald LL, Zheng H, Weimer J, Boada FE. Sodium imaging of human brain at 7 T with 15-channel array coil. *Magn Reson Med.* 2012; 68:1807–1814.
31. Qian Y, Zhao T, Lakshmanan K, Ge Y, Lui Y, Shepherd T, Boada FE. Proof of concept for the separation of free and bound sodium in human brain through two-TE acquisitions at 3T. In the Proceedings of the 25th Annual Meeting of ISMRM, Honolulu, Hawaii, USA, 2017. p. 6355.
32. Boada FE, Gillen JS, Shen GX, Chang SY, Thulborn KR. Fast three-dimensional sodium imaging. *Magn Reson Med.* 1997; 37:706–715.
33. Jackson JI, Meyer CH, Nishimura DG, Macovski A. Selection of a convolution function for Fourier inversion using gridding. *IEEE Trans Med Imaging.* 1991; 10:473–478.
34. Hoge RD, Kwan KS, Pike GB. Density compensation functions for spiral MRI. *Magn Reson Med.* 1997; 38:117–128.
35. Roemer PB, Edelstein WA, Hayes CE, Souza SP, Mueller OM. The NMR phased array. *Magn Reson Med.* 1990; 16:192-225.
36. Robinson S, Jovicich J. B_0 mapping with multi-channel RF coils at high field. *Magn Reson Med.* 2011; 66:976–988.
37. Haacke EM, Brown RW, Thompson MR, Venkatesan R. Magnetic resonance imaging - Physical principles and sequence design. New York: John Wiley & Sons, Inc; 1999. 914 p.
38. Goldstein I, Lerer E, Laiba E, Mallet J, Mujaheed M, Laurent C, Rosen H, Ebstein RP, Lichtstein D. Association between sodium-and potassium-activated adenosine triphosphatase α isoforms and bipolar disorders. *Biological psychiatry.* 2009; 65:985-991.
39. Carvalho AF, Firth J, Vieta E. Bipolar disorder. *N Engl J Med.* 2020; 383:58–66.
40. Blunck Y, Josan S, Taqdees SW, Moffat BA, Ordidge RJ, Cleary JO, Johnston LA. 3D-multi-echo radial imaging of ^{23}Na (3D-MERINA) for time-efficient multi-parameter tissue compartment mapping. *Magn Reson Med.* 2018; 79:1950-1961.
41. Lommen JM, Flassbeck S, Behl NG, Niesporek S, Bachert P, Ladd ME, Nagel AM. Probing the microscopic environment of ^{23}Na ions in brain tissue by MRI: on the accuracy of

- different sampling schemes for the determination of rapid, biexponential decay at low signal-to-noise ratio. *Magn Reson Med.* 2018; 80:571-584.
42. Leroi L, Coste A, de Rochefort L, Santin MD, Valabregue R, Mauconduit F, Giacomini E, Luong M, Chazel E, Valette J, Le Bihan D. Simultaneous multi-parametric mapping of total sodium concentration, T1, T2 and ADC at 7 T using a multi-contrast unbalanced SSFP. *Magn Reson Med.* 2018; 53:156-163.
 43. Alhulail AA, Xia P, Shen X, Nichols M, Volety S, Farley N, Thomas MA, Nagel AM, Dydak U, Emir UE. Fast in vivo ^{23}Na imaging and mapping using accelerated 2D-FID UTE magnetic resonance spectroscopic imaging at 3 T: Proof of concept and reliability study. *Magn Reson Med.* 2021; 85:1783-1794.
 44. Ridley B, Nagel AM, Bydder M, Maarouf A, Stellmann JP, Gherib S, Verneuil J, Viout P, Guye M, Ranjeva JP, Zaaraoui W. Distribution of brain sodium long and short relaxation times and concentrations: a multi-echo ultra-high field ^{23}Na MRI study. *Scientific reports.* 2018; 8(1):4357.
 45. Kratzer FJ, Flassbeck S, Schmitter S, Wilferth T, Magill AW, Knowles BR, Platt T, Bachert P, Ladd ME, Nagel AM. 3D sodium (^{23}Na) magnetic resonance fingerprinting for time-efficient relaxometric mapping. *Magn Reson Med.* 2021; 86:2412-2425.
 46. Syeda W, Blunck Y, Kolbe S, Cleary JO, Johnston LA. A continuum of components: Flexible fast fraction mapping in sodium MRI. *Magn Reson Med.* 2019; 81:3854-3864.
 47. Riemer F, Solanky BS, Wheeler-Kingshott CA, Golay X. Bi-exponential ^{23}Na T2* component analysis in the human brain. *NMR in Biomedicine.* 2018; 31(5):e3899.
 48. Qian Y, Zhao T, Lakshmanan K, Ge Y, Lui Y, Shepherd T, Boada FE. Proof of concept for the separation of free and bound sodium in human brain through two-TE acquisitions at 3T. In the Proceedings of the 25th Annual Meeting of ISMRM, Honolulu, Hawaii, USA, 2017. p. 6355.
 49. Winter PM, Bansal N. TmDOTP5—as a ^{23}Na shift reagent for the subcutaneously implanted 9L gliosarcoma in rats. *Magnetic Resonance in Medicine.* 2001;45(3):436-442.

11. FIGURES

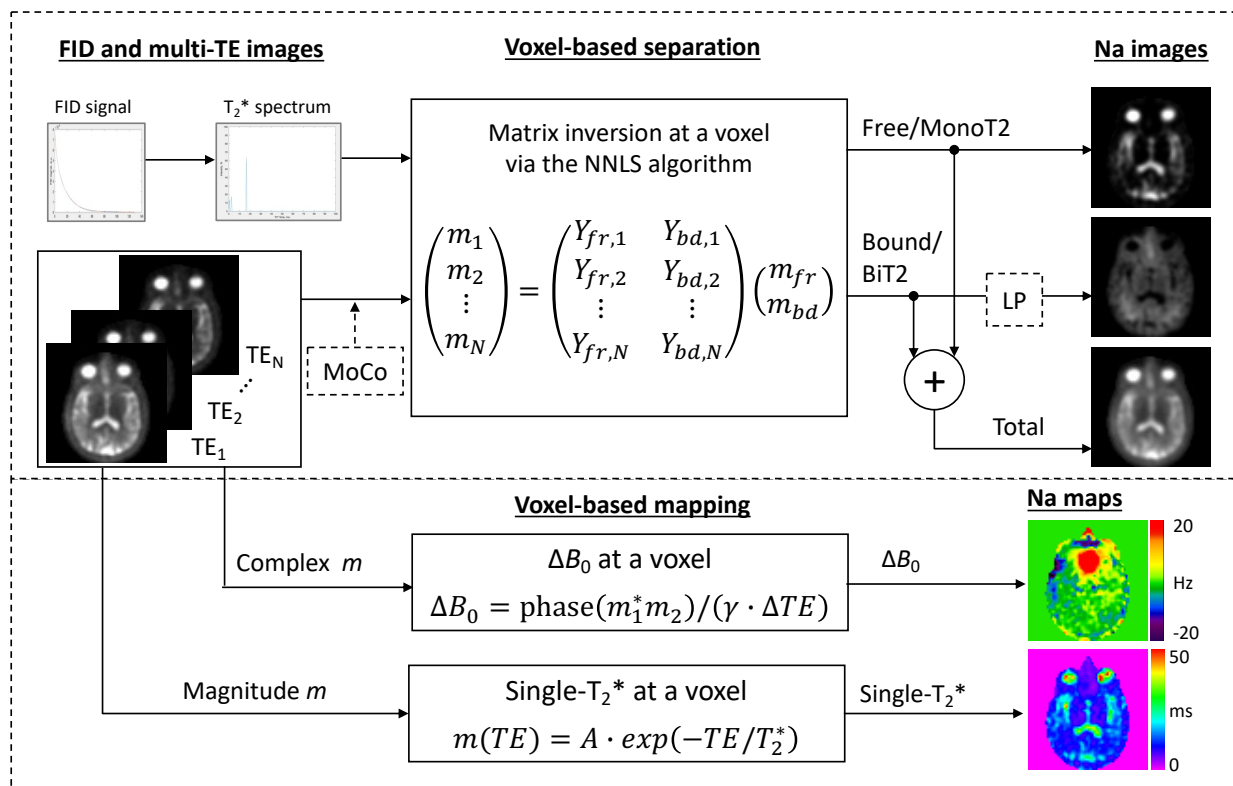


Fig. 1. Flowchart of the proposed MSQ sodium MRI (light green portion). **Input:** Multi-TE SQ images $m(TE)$ and an FID signal producing T_2^* spectrum. Motion correction (MoCo) between SQ images is optional. **Separation:** Matrix inversion voxel-by-voxel across the field-of-view (FOV). **Output:** Three sodium images (free m_{fr} , bound m_{bd} , and total $m_{fr}+m_{bd}$). The low-pass (LP) filtering (optional) is a 3D smoothing of size 3x3x3 or others, to further reduce random noise. **Additional outputs** (light pink portion) are the maps of B_0 inhomogeneity and single- T_2^* , which provide complimentary information for the quantification and interpretation on the free (mono- T_2) and bound (bi- T_2) sodium images.

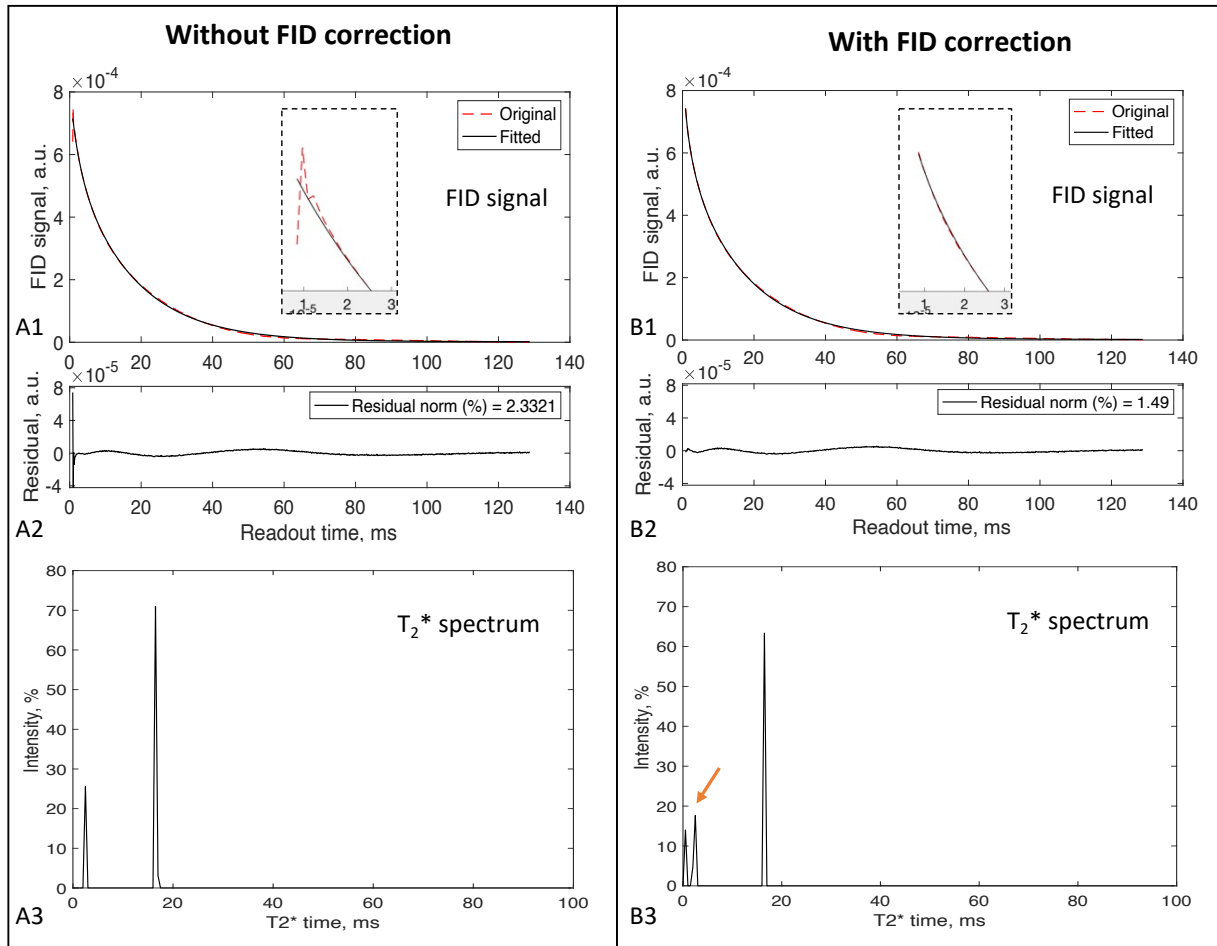


Fig. 2. FID signals (top row) and T_2^* spectra (bottom row) from whole brain of a healthy subject (52 years old, male), with (right column, light green) and without (left column, light pink) the correction for FID distortion at the first five samples shown in the insets. In the middle row are the residual errors from the fitting using the T_2^* spectra in the bottom row. The FID correction removed the distortion, significantly reduced the residual error, and clearly improved resolution of short- T_2^* components from singlet at 2.5ms to doublet at 0.5ms and 2.5ms as well as peaks' intensity (bottom right, orange arrow). Data acquisition: 3T scanner (Prisma, Siemens) with a custom-built dual-tuned (^1H - ^{23}Na) 8-channel head array coil, *fid* sequence, rectangular RF duration = 0.5ms, TE/TR=0.35/300ms, averages=128, ADC samples=1024 at an interval of 0.125ms.

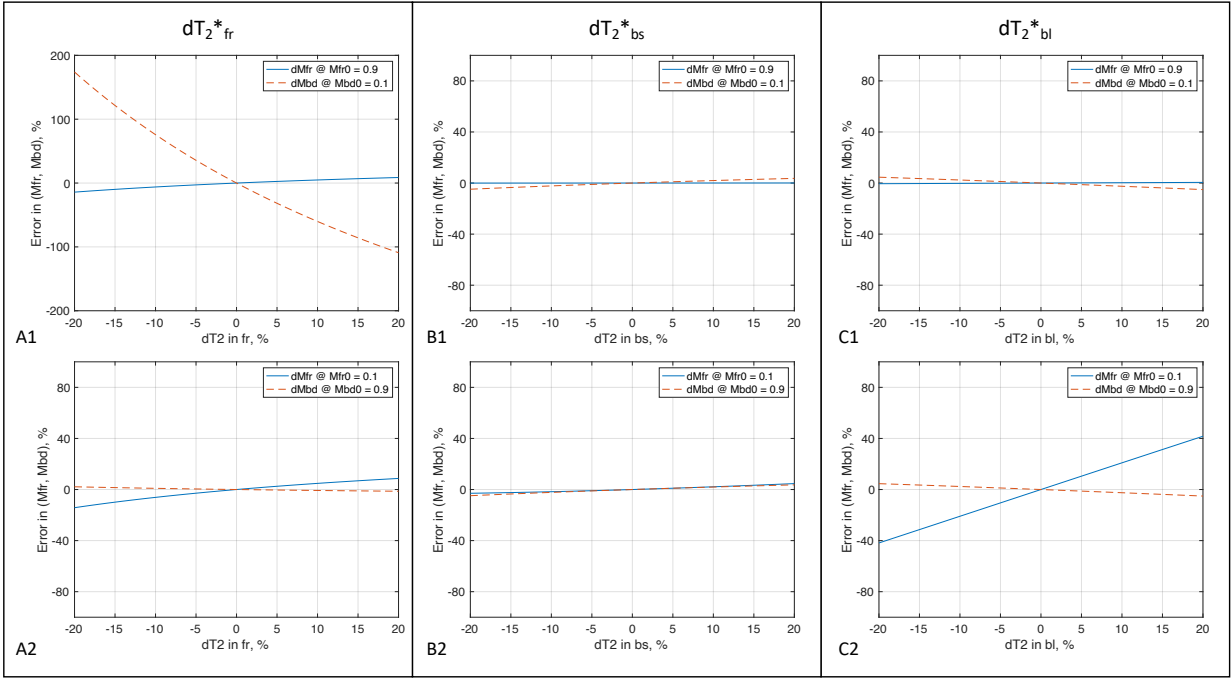


Fig. 3. Simulated impact of T_2^* values on the separation of free (mono- T_2) and bound (bi- T_2) sodium signals (m_{fr} , m_{bd}) at a typical set of $(T_2^*_{fr}, T_2^*_{bs}, T_2^*_{bl}) = (50.0, 3.5, 15.0)$ ms in two extreme cases: the free sodium dominating (top row), $m_{fr} = 0.9$, and the bound sodium dominating (bottom row), $m_{bd} = 0.9$. In the columns are the impact of individual T_2^* components. **A)** An error in $T_2^*_{fr}$ produced an error in m_{fr} or m_{bd} much smaller for the dominant one (e.g., $\Delta m_{bd} < 2.2\%$ when $\Delta T_2^*_{fr} < 20\%$, and $\Delta m_{fr} < 2.9\%$ when $\Delta T_2^*_{fr} < 5.0\%$). **B)** An error in $T_2^*_{bs}$ had a small impact on both m_{fr} and m_{bd} (e.g., when dominating, $\Delta m_{bd} < 4.8\%$ and $\Delta m_{fr} < 0.04\%$ when $\Delta T_2^*_{bs} < 20\%$). **C)** An error in $T_2^*_{bl}$ led to an error in m_{fr} or m_{bd} much smaller for the dominant one (e.g., $\Delta m_{bd} < 5.2\%$ and $\Delta m_{fr} < 0.6\%$ when $\Delta T_2^*_{bl} < 20\%$). The best case is Column B where the $T_2^*_{bs}$ had small impact ($< 4.9\%$) on both free and bound sodium signals. The worst case is A1) where the $T_2^*_{fr}$ had a large impact on the bound sodium signal, $\Delta m_{bd} = 35.6\%$ when $\Delta T_2^*_{fr} = -5\%$.

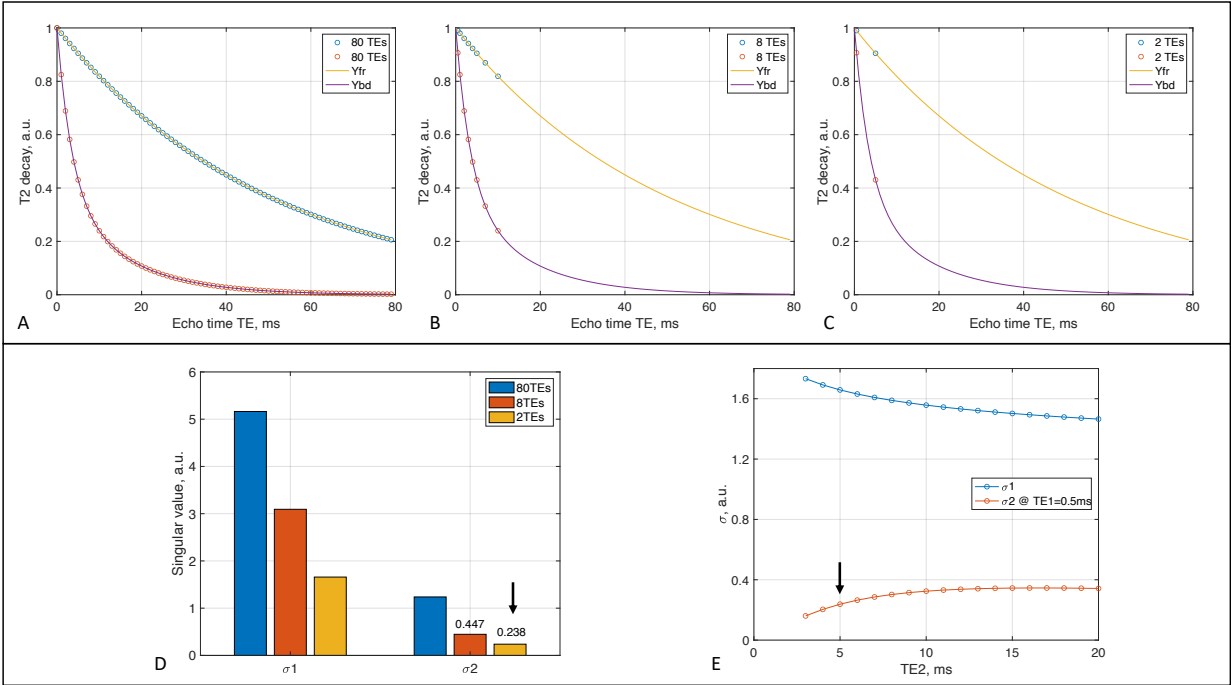


Fig. 4. TE scheme optimization via SVD singular values. **A)** A reference scheme of 80 TEs in a range of 0–79ms at an interval of 1.0ms, distributing on a mono-exponential T_2^* decay $Y_{fr}(TE)$ of the free sodium at a typical $T_2^*_{fr}=50$ ms, and on a bi-exponential T_2^* decay $Y_{bd}(TE)$ of the bound sodium at a typical set $\{T_2^*_{bs}, T_2^*_{bl}\} = \{3.5, 15.0\}$ ms. **B)** An intuitively-favorable scheme of 8 TEs at $\{0.5, 1, 2, 3, 4, 5, 7, 10\}$ ms, distributing on the decay curves Y_{fr} and Y_{bd} . **C)** The optimal scheme of 2 TEs at $\{0.5, 5\}$ ms, distributing on the decay curves Y_{fr} and Y_{bd} . **D)** The SVD singular values (σ_1 and σ_2) of the three TE schemes. **E)** Singular values of the 2-TEs scheme changing with the 2nd TE (or TE_2). In D, σ_2 is less than 1.0 at the 8-TEs and 2-TEs, leading to noise amplification. Thus, a better choice for less noise amplification is the 2-TEs (arrow). In E, TE_2 at 5ms (arrow) produced a value near maximum for σ_2 while preserving higher signal than the larger TE_2 . Therefore, the 2-TEs scheme is an optimal one for the human brain.

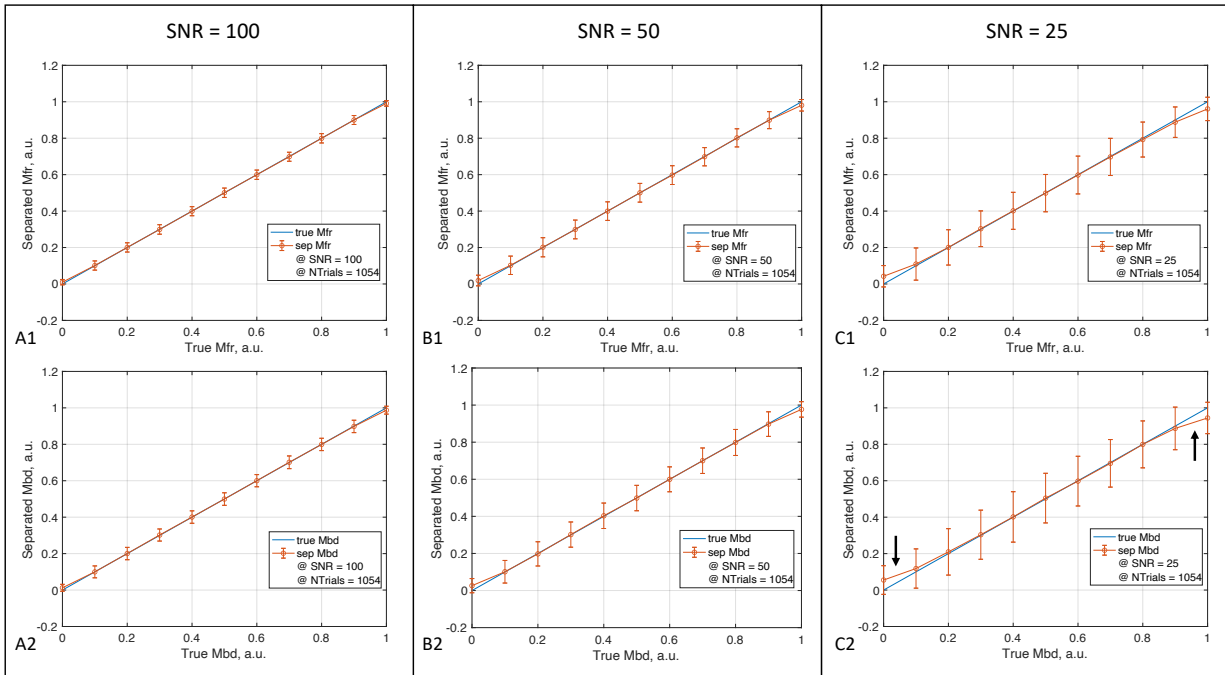


Fig. 5. Simulated separation of the free and bound sodium signals (m_{fr} , m_{bd}) at a typical set of $(T_2^*_{fr}, T_2^*_{bs}, T_2^*_{bl}) = (50.0, 3.5, 15.0)$ ms and 2-TE scheme TEs=(0.5, 5.0). **A)** Extra-high SNR=100, **B)** High SNR=50, and **C)** Regular SNR=25. The standard deviation (error bar) of the separated m_{fr} (top row) and m_{bd} (bottom row) consistently decreased with SNR increasing from 25 to 100. There was an underestimate (3.9–5.6%, arrow) for m_{fr} or m_{bd} near the maximum value 1.0, but an overestimate (4.2–5.5%, arrow) near the minimum value 0.0, with an amount decreasing with SNR increasing.

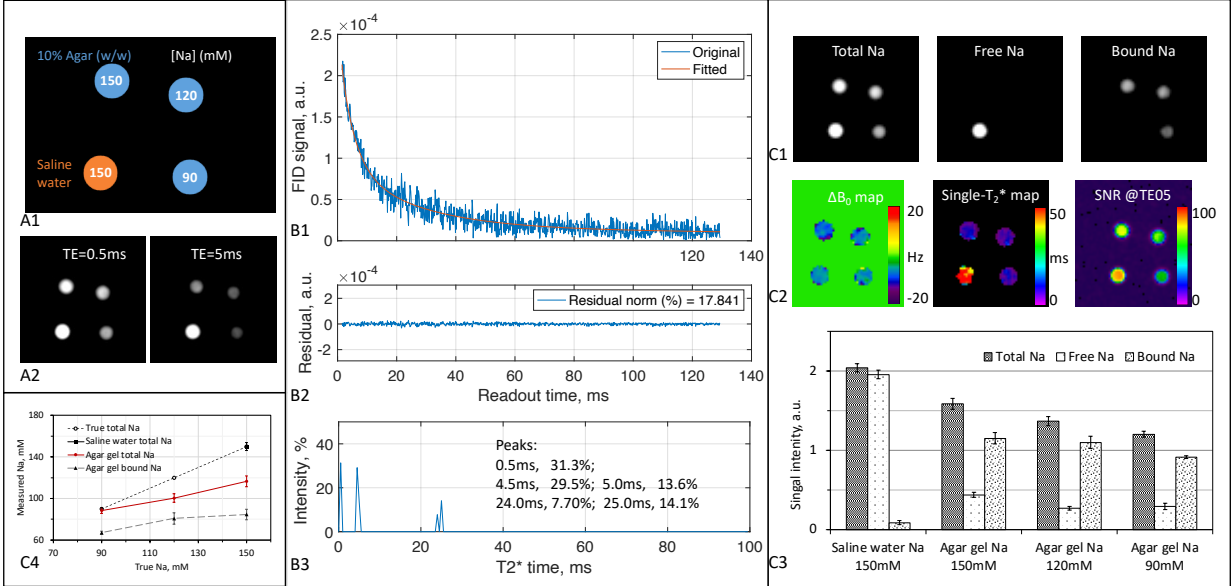


Fig. 6. Phantom study. **A1)** Phantom of four tubes with sodium concentration: 150mM for the saline water and 90, 120, 150 mM for the agar gels. **A2)** Sodium images of the phantoms at TE1/TE2=0.5/5ms, shown in the same window/level. **B1)** FID signals (original and fitted) from the four tubes at averages=1, with the correction for distortion at the first five data points. **B2)** Residual error of the fitting in B1. **B3)** T_2^* spectrum calculated from the original FID in B1 and used to produce the fitted FID. **C1)** Sodium images (total, free, and bound) separated from the two images in A2 at $(T_2^*_{fr}, T_2^*_{bs}, T_2^*_{bl}) = (50, 5, 25)$ ms according to B3 and C2. **C2)** Maps of ΔB_0 and single- T_2^* calculated from the two images in A2, and map of SNR at TE=0.5ms. **C3)** Separated sodium signals in the tube regions in C1. **C4)** Quantified sodium concentration from C3.

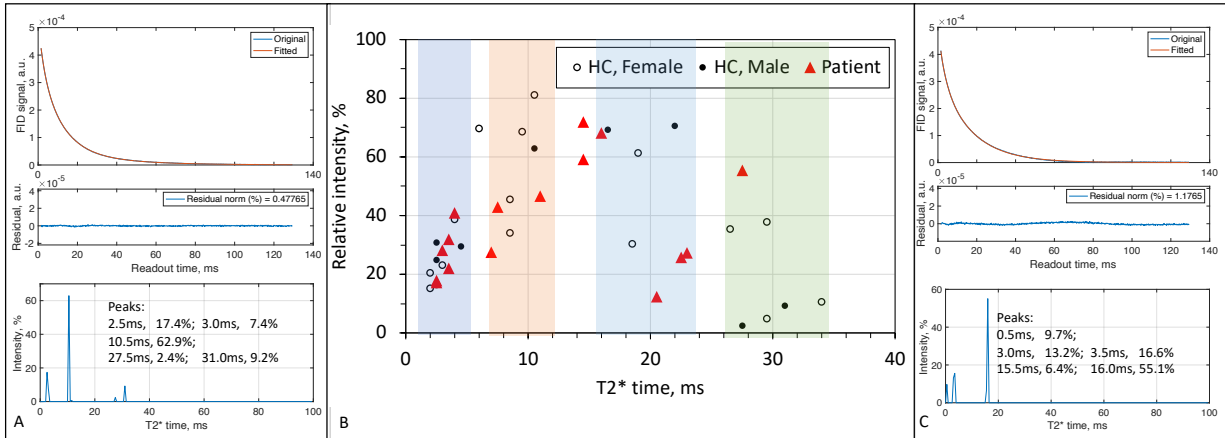


Fig. 7. Human study: a 2D scattering plot of individual T_2^* components from the T_2^* spectra and relative intensity (%), across all the subjects studied. **A)** Typical T_2^* spectrum, and associated FID signal and fitting error, from the whole brain of a healthy young subject (21 years old, male). **B)** Scattering plot of individual T_2^* components in the subjects' brains. **C)** Another typical T_2^* spectrum from an epilepsy patient (31 years old, male).

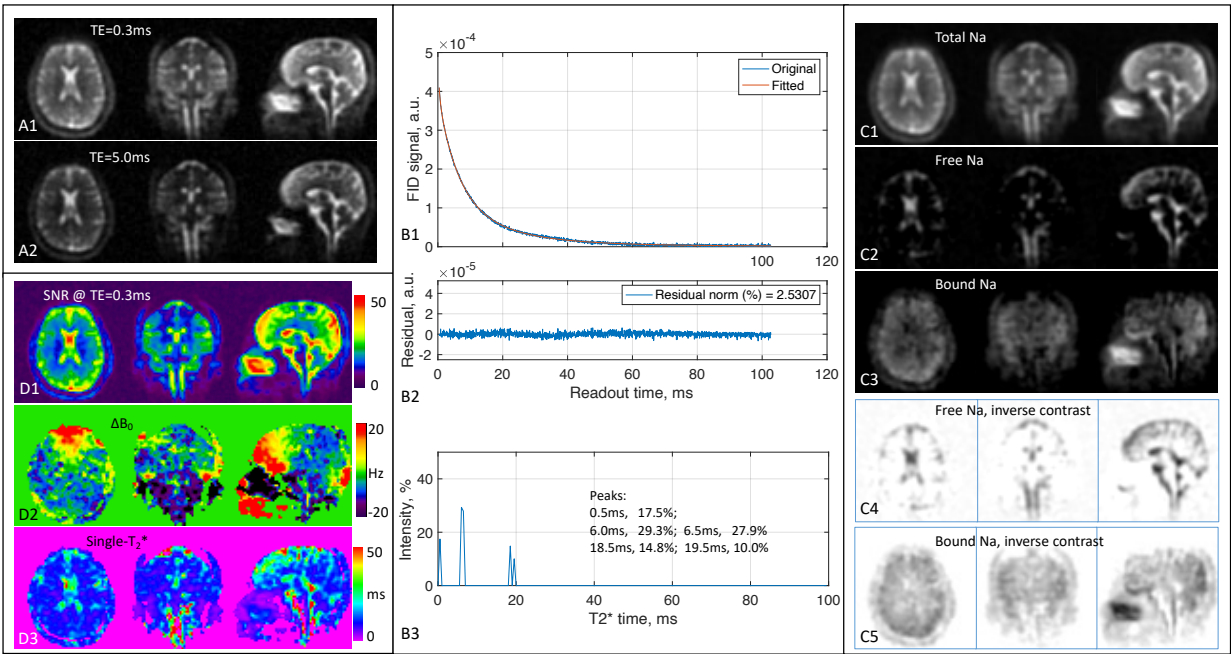


Fig. 8. Human study #1 (26-year-old female, healthy). **A)** 3D sodium images of the brain in three orthogonal slices at TE₁/TE₂=0.3/5ms. **B)** FID signal of the whole brain and associated fitting error and T₂^{*} spectrum. **C)** Separated sodium images from the 2-TE images in A), using (T₂^{*}_{fr}, T₂^{*}_{bs}, T₂^{*}_{bl}) = (50.0, 6.0, 19.0)ms according to B3. In C4-C5 are inverse-contrast display to highlight low intensity. All the images in A and C were displayed in the same window/level. **D)** Maps of SNR, ΔB₀, and single-T₂^{*}, calculated from the 2-TE images in A.

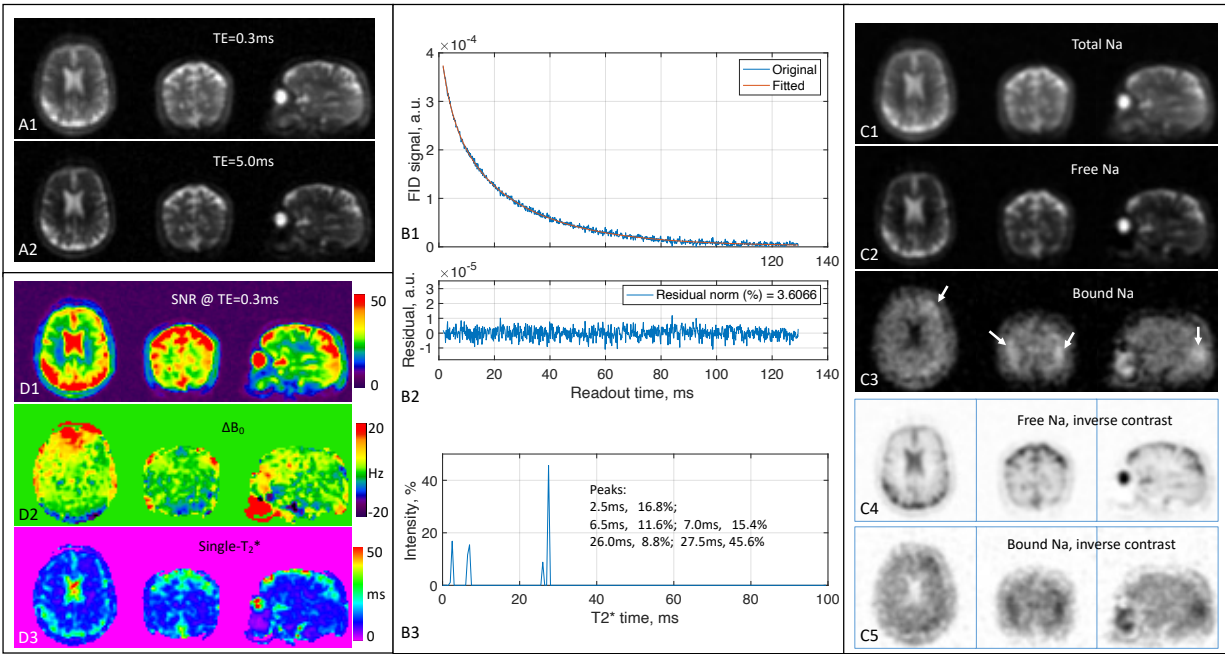


Fig. 9. Human study #2 (59-year-old male, bipolar disorder patient). **A)** 3D sodium images of the brain at $TE_1/TE_2=0.3/5$ ms. **B)** FID signal of the whole brain and associated fitting error and T_2^* spectrum. **C)** Separated sodium images from the 2-TE images in A), using $(T_2^{*fr}, T_2^{*bs}, T_2^{*bl}) = (50.0, 2.5, 7.0)$ ms according to peaks in B3). In C4-C5 are inverse-contrast display of C2-C3 to highlight low intensity. All the images in A) and C) were displayed in the same window/level, except C3 and C5 where W/L was halved. **D)** Maps of SNR, ΔB_0 , and single- T_2^* , calculated from the 2-TE images in A). Note that bound sodium images in C3 (or C5) clearly highlighted brain regions (arrows) with an elevated bound sodium concentration.

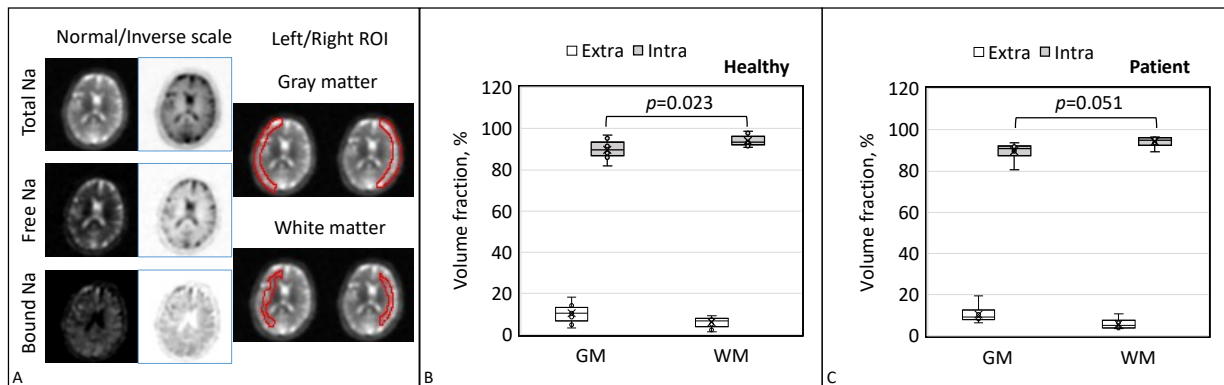


Fig. 10. The up-band volume fraction of extra- and intracellular spaces by assigning all the free sodium into extracellular space at $C_{ex}=145\text{mM}$ and all the bound sodium into intracellular space at $C_{in}=15\text{mM}$. **A)** Typical sodium images (total, free, and bound) and regions of interest (ROIs) for the gray matter (GM) and white matter (WM) in a slice of a healthy subject. **B)** Volume fractions for the healthy group ($n=9$). **C)** Volume fractions for the patient group ($n=6$). **Note:** the difference in volume fraction is statistically significant between the gray and white matters ($P=0.023$) for the healthy group, but not for the patient group ($P=0.051$). It is not significant between the healthy and patient groups for the gray or white matter ($P=0.953$).

12. Supporting Information

Separation of Sodium Signals Between Mono- and Bi-Exponential T_2 Decays via Multi-TE
Single-Quantum Sodium (^{23}Na) MRI

Supporting Information

Yongxian Qian,¹ Ying-Chia Lin,¹ Xingye Chen,^{1,2} Tiejun Zhao,³ Karthik Lakshmanan,¹ Yulin Ge,¹ Yvonne W. Lui,^{1,4} Fernando E. Boada^{1,5}

¹ Bernard and Irene Schwartz Center for Biomedical Imaging, Department of Radiology, New York University Grossman School of Medicine, New York, NY 10016.

² Vilcek Institute of Graduate Biomedical Sciences, NYU Grossman School of Medicine, New York, NY 10016.

³ Siemens Medical Solutions USA, New York, NY 10016.

⁴ Department of Radiology, NYU Langone Health, New York, NY 10016.

⁵ Now at Department of Radiology, Stanford University, Stanford, CA 94305.

Correspondence: Yongxian Qian, PhD

Center for Biomedical Imaging (CBI)

660 First Ave, 4th Floor

New York, NY 10016, USA

Phone: 212-263-1159

Email: Yongxian.Qian@nyulangone.org

S1. The calculation stability of T_2^* spectrum at a high resolution of $\Delta T_2^*=0.5\text{ms}$

T_2^* spectrum was calculated via Eq. [4] on an FID signal using an established algorithm called non-negative least squares (NNLS) at a high spectral resolution of $\Delta T_2^*=0.5\text{ms}$ in a range of 0.5–100ms. This high resolution raises a concern on stability of the calculation as the base functions at these spectral locations, $\exp(-t/T_2^*)$, are not independent. To address this concern, 1) we employed the singular value decomposition (SVD) to analyze the transfer matrix E , and 2) we used numerical simulations to detail the impact of random noise on the T_2^* spectrum.

S1.1. VSD analysis on the transfer matrix E

$$E_{i,j} \equiv \exp(-t_i/T_{2,j}^*), \quad i = 1, 2, \dots, N, \quad j = 1, 2, \dots, M, \quad N \gg M \quad \text{Eq. [S1.1.1]}$$

$$\mathbf{E}^T \mathbf{E} = \mathbf{U} \mathbf{\Sigma} \mathbf{V}^T \quad \text{Eq. [S1.1.2]}$$

$$\mathbf{\Sigma} = \text{diag}(\sigma_1, \sigma_2, \dots, \sigma_M) \quad \text{Eq. [S1.1.3]}$$

with sampling time $t_i = TE + (i - 1) * \Delta t$ and spectral point $T_{2,j}^* = j * \Delta T_2^*$. Singular values $\{\sigma_j, j = 1, 2, \dots, M\}$ determine stability of the calculation for T_2^* spectrum in terms of noise interference in Eq. [4]. Correlation coefficients between the base functions are also calculated.

$$R_{j1,j2} = (E^T E)_{j1,j2} / \sqrt{(E^T E)_{j1,j1} (E^T E)_{j2,j2}}, \quad j1, j2 = 1, 2, \dots, M \quad \text{Eq. [S1.1.4]}$$

At $\Delta t = 0.05\text{ms}$, $TE=0.2\text{ms}$ and $N=2048$, the singular values and correlation coefficients were calculated and illustrated in Fig. S1.1. The singular value σ quickly decreases to zero ($<10^{-10}$) at index (15, 13, 10, 9) when ΔT_2^* increases from 0.5ms to 1.0, 3.0 and 5.0ms, respectively. This indicates the existence of null subspace or multiple solutions for T_2^* spectrum (Fig. S1.1, top). The normalized correlation coefficients R between any two T_2^* base functions is spreading away from diagonal line, confirming non-orthogonal between the base functions (Fig.S1.1, bottom). However, the extent of spreading is narrower for short T_2^* values at high resolution $\Delta T_2^* = 0.5\text{ms}$ than at low resolution $\Delta T_2^* = 5\text{ms}$.

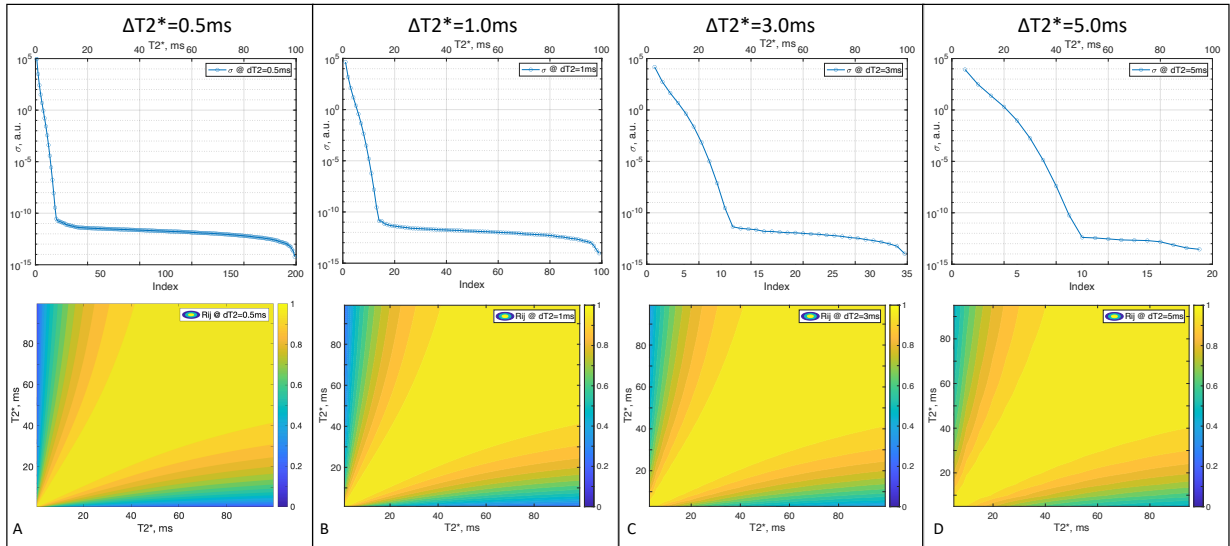


Fig. S1.1. Calculation stability of T_2^* spectrum using SVD analysis on matrix $E^T E$ (top) and the base-correlation on matrix E (bottom). **A) – D)** T_2^* spectral resolution at $\Delta T_2^* = 0.5, 1.0, 3.0,$ and 5.0ms . In the top, singular value σ quickly decreases to zero ($<10^{-10}$) at index (15, 13, 10, 9) respectively, indicating the existence of null subspace or multiple solutions for the T_2^* spectrum. In the bottom, the normalized correlation coefficient $R_{j1,j2}$ between any two T_2^* base functions $\exp(-t/T_{2,j}^*)$ is spreading away from diagonal line, showing non-orthogonal between the base functions.

S1.2. Numerical simulation for the impact of random noise on the T_2^* spectrum

The simulation was performed at three popular components, $T_2^*=(3, 15, 50)$ ms with relative amplitudes $A=(30, 20, 50)$, with an additive normal random noise generated by function $randn(n,1)$, at SNR=100, 50, and 25. Outcomes of the simulation were summarized in Fig. S1.2, where the peak parameters at doublets (Fig. S1.2, bottom) were linearly combined with amplitude-weighting by the left- and right-peaklets (Eq. S1.2).

$$T_2^* = (A_L * T_{2,L}^* + A_R * T_{2,R}^*)/A \quad \text{Eq. [S1.2.1]}$$

$$A = A_L + A_R \quad \text{Eq. [S1.2.2]}$$

The best spectrum was achieved at SNR=100 among the three noisy cases, relative to no-noise.

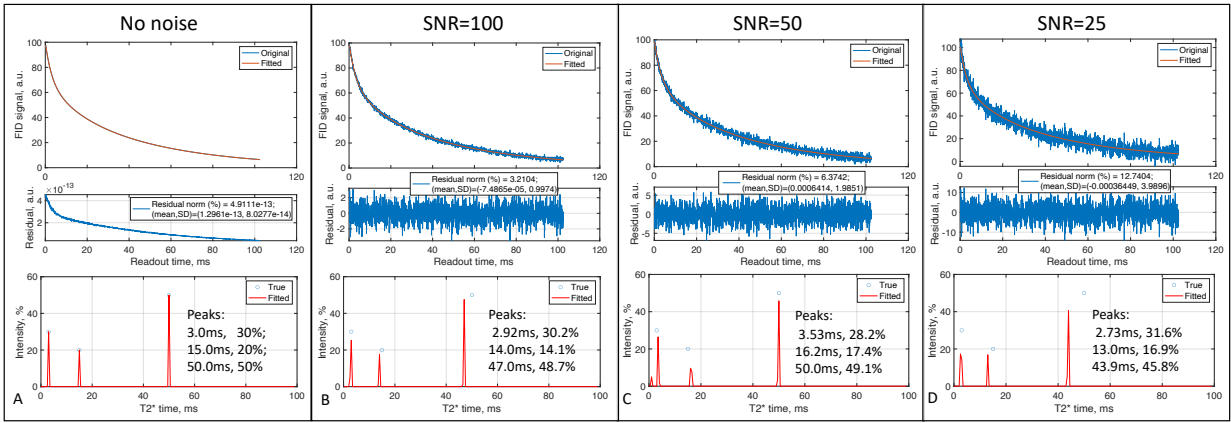


Fig. S1.2. Calculation stability of T_2^* spectrum using the algorithm NLS via MATLAB function $lsqnonneg(C,d)$ and the numerical simulations at three popular components: $T_2^*=(3, 15, 50)$ ms with relative amplitudes $A=(30, 20, 50)$ and an additive random noise generated by function $randn(n,1)$. **A) - D)** are the simulations at $\Delta T_2^* = 0.5$ ms with noise at three typical values SNR = 100, 50, and 25. The peak parameters at doublets (bottom) were linearly combined with amplitude-weighting (Eq. S1.2.1). The best spectrum was achieved at SNR=100 among the three noisy cases.

S2. The measurement stability of FID signals on whole brain: B_0 shimming

The B_0 shimming may change from subject to subject, leading to a concern on the measurement stability of FID signals, thus the T_2^* spectra, from whole brain. This concern is addressable because 1) sodium (^{23}Na) MRI has a 4-times lower resonance frequency than proton (^1H) MRI (e.g., 33.8 vs. 127.7 MHz at 3T), and 2) a manual shimming (three iterations) is better than auto shimming. Fig. S2 presents results of all the 15 subjects studied, with a small standard deviation (SD) in whole-brain histograms. There was no significant difference between the healthy and patient groups ($P=0.908$). Thus, the manual shimming, or ΔB_0 , is stable.

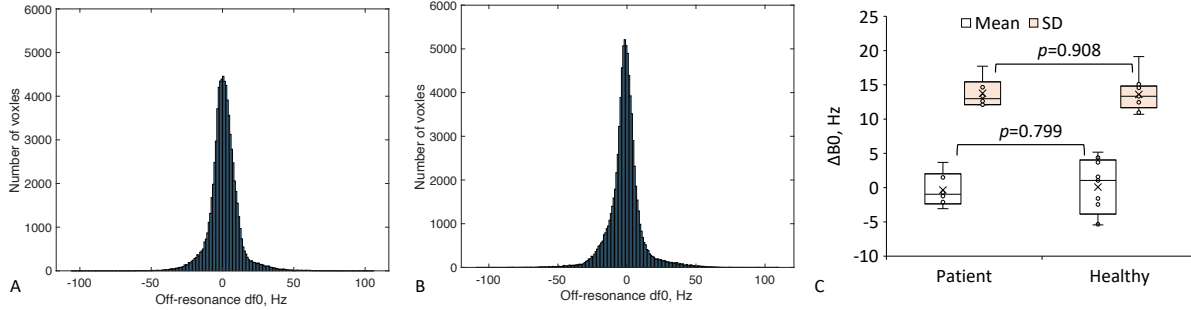


Fig. S2. Whole-brain histograms of ΔB_0 mapping at TE1/TE2= 0.5/5ms under a manual shimming procedure. **A)** Representative histogram from a healthy subject (52 years old, male), with mean \pm SD = 1.0 \pm 10.7 Hz. **B)** Representative histogram from an epilepsy patient (31 years old, male), with mean \pm SD = -1.2 \pm 12.1 Hz. **C)** Mean and SD distribution of whole-brain ΔB_0 histograms from all the 9 healthy and 6 patients studied, showing no significant difference between the two groups (healthy vs. patient), $P = 0.799$ for the mean and $P = 0.908$ for the SD.

S3. The invisibility of CSF T_2^* peak in the spectrum: single T_2^* mapping

CSF in the brain is known to have a T_2^* value of ~ 50 ms as seen in single- T_2^* maps (Figs. 8,9). But this sodium population was not observed in the T_2^* spectra. This phenomenon might be caused by small volume of CSF relative to whole brain. To confirm this cause, Fig. S3 presents two representative whole-brain histograms of single- T_2^* mapping, with very small numbers of voxels (invisible bins) for CSF at $T_2^* \sim 50$ ms.

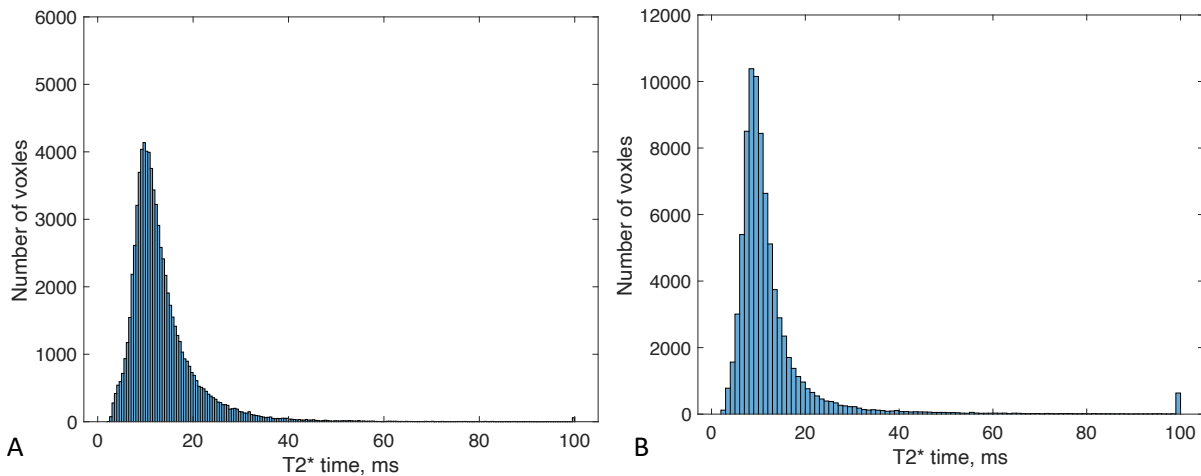


Fig. S3. Representative whole-brain histograms of single- T_2^* mapping at TE1/TE2= 0.5/5ms. **A)** A healthy subject (52 years old, male). **B)** An epilepsy patient (31 years old, male). These, as well as the other healthy subjects and patients studied, showed very small numbers (invisible bins) of voxels for CSF at $T_2^* \sim 50$ ms. Note: a visible bin at $T_2^*=100$ ms counts voxels of T_2^* values ≥ 100 ms.